Top-down estimate of regional carbon sinks over East Asia for 2010–2019 using satellite observations

Mina Kim[1], Rokjin J. Park[1*], Jingi Jung[1], Sang-Ik Oh[1], Eunjo S. Ha[1], Jaein I. Jeong[1], Sang-Wook Yeh[2]

[1]School of Earth and Environmental Science, Seoul National University, Seoul, Republic of Korea
[2]Department of Marine Sciences and Convergent Engineering, Hanyang University, ERICA, Seoul, Republic of Korea

Correspondence to: Rokjin J. Park (rjpark@snu.ac.kr)

Abstract. East Asia is a major source of fossil fuel emissions and strongly influences regional and global CO_2 concentrations. Quantifying natural carbon sinks in this region is therefore essential for improving climate projections and informing mitigation strategies. We estimated the Net Ecosystem Exchange (NEE) and ocean carbon fluxes over East Asia (18.5°N–54°N, 73°E–146°E) during 2010–2019 using a Bayesian inversion framework. The GEOS-Chem chemical transport model was combined with GOSAT ACOS v9 XCO_2 retrievals, and region-specific prior uncertainties were assigned using standard deviations from land and ocean models. Posterior estimates show enhanced carbon uptake relative to the prior, with NEE increasing from −0.17 ± 0.08 to −0.31 ± 0.06 PgC yr^{-1} and ocean uptake changing slightly from −0.20 ± 0.03 to −0.21 ± 0.03 PgC yr^{-1}. Simulated CO_2 concentrations based on posterior fluxes agreed better with independent observations than those from prior fluxes. East Asia's terrestrial ecosystems exhibited net carbon uptake during 2010–2019, consistent with increasing Enhanced Vegetation Index (EVI) trends. However, several regions showed temporary positive NEE during 2015–2016, likely linked to the strong 2015/16 El Niño. When fossil fuel and biomass burning are included, East Asia released a net flux of +3.45 PgC yr^{-1} to the atmosphere during 2010–2019. Natural sinks offset only ~13.6% of fossil fuel emissions, leaving a substantial residual source. Despite increased posterior sinks, they remain insufficient to counter regional emissions, sustaining elevated CO_2 levels and continued outflow from East Asia.

1 Introduction

Carbon dioxide (CO_2) is the most important anthropogenic greenhouse gas (GHG), with atmospheric concentrations having risen from the pre-industrial level of 280 ppm to 426 ppm in 2025 (Joos and Spahni, 2008; Lan et al., 2025). To achieve the Paris Agreement's goal of limiting global temperature rise to below 1.5 °C above pre-industrial levels (UNFCCC, 2015), effective carbon management is imperative. This entails not only controlling anthropogenic emissions but also improving our understanding of carbon sink mechanisms, as major natural sinks such as terrestrial ecosystems and oceans currently absorb roughly half of global emissions (Friedlingstein et al., 2023). Net Ecosystem Exchange (NEE) represents the net CO_2 exchange between terrestrial ecosystems and the atmosphere and reflects the balance between photosynthetic uptake and ecosystem respiration. It is widely used to quantify the strength of land carbon sinks (Lian et al., 2023; Munassar et al., 2022; Reichstein

et al., 2005). In parallel, air–sea CO_2 flux describes the net exchange of CO_2 between the ocean and the atmosphere and constitutes a major component of the global carbon budget. However, significant uncertainties remain regarding the capacity and dynamics of these natural sinks (IPCC, 2023). This problem is particularly acute in East Asia, one of the world's fastest-growing carbon-emitting regions (Gilfillan and Marland, 2021). Despite its critical role, previous studies have struggled to accurately estimate regional carbon fluxes due to the limited number of in situ CO_2 observation sites in Asia compared to Europe or North America (Park and Kim, 2020), which poses a limitation for robust regional carbon flux estimation.

Carbon fluxes are commonly estimated using two main approaches: bottom-up and top-down. Bottom-up methods combine observations with statistical upscaling or process-based models (Jung et al., 2020; Kondo et al., 2020; Sitch et al., 2008, 2015). In contrast, top-down methods infer surface fluxes by applying inverse techniques to atmospheric CO_2 concentration data, a process commonly referred to as atmospheric inverse modeling. Among top-down techniques, atmospheric inversions driven by a chemical transport model (CTM) are widely used (Basu et al., 2018; Nassar et al., 2011; Palmer et al., 2003; Peylin et al., 2013). Building on these approaches, international efforts to quantify regional carbon fluxes have continued. REgional Carbon Cycle Assessment and Processes (RECCAP) is an international initiative aimed at quantifying regional greenhouse gas budgets, including CO_2 (Canadell et al., 2011). Coordinated assessments have also been conducted for East Asia. In particular, Wang et al. (2024) provided a comprehensive evaluation of greenhouse gas budgets over East Asia for the 2000s and 2010s using both top-down and bottom-up approaches. In their framework, the top-down estimates represented integrated net land–atmosphere CO_2 fluxes at the regional scale rather than NEE alone. Bottom-up NEE estimates were also reported, although these were based on the TRENDY v9 dynamic global vegetation model ensemble (Sitch et al., 2015) rather than being newly derived within that study. These estimates are briefly compared with the results of this study in Section 5.

While several studies have examined carbon fluxes in East Asia, most have either focused on China or provided only limited quantitative assessments of flux uncertainties. For example, Wang et al. (2020) estimated Chinese carbon fluxes from in situ data, assigning prior uncertainties of 50% for land and 40% for ocean, which were prescribed as simple percentage values rather than derived from data variability. Thompson et al. (2016), as part of the RECCAP initiative, used a seven-model inversion ensemble for Asia, but applied inconsistent prior fluxes and uncertainties across models. Jiang et al. (2013) estimated carbon uptake in China using ground observations. In their framework, land prior uncertainties were derived from net primary production, while a uniform prior uncertainty was assumed for the ocean.

Since in situ CO_2 measurements are highly precise (typical observational errors <0.2 ppm), they have been extensively used in inversion frameworks (Baker et al., 2006; Deng and Chen, 2011; Gurney et al., 2003; Jiang et al., 2013; Monteil et al., 2020; Peylin et al., 2013). Their major limitation is sparse spatial coverage, especially over data-poor regions such as the oceans and much of Africa. Satellite retrievals, by contrast, offer broad spatial coverage. The Greenhouse Gases Observing SATellite (GOSAT), launched in 2009, provides global column-averaged CO_2 (XCO_2) observations. GOSAT has a footprint of approximately 10.5 km in diameter with an observation error of about 1 ppm (Kulawik et al., 2019). Whereas Wang et al. (2019) excluded oceanic soundings due to large uncertainties associated with glint-mode retrievals (Wunch et al., 2017), such

exclusions may not be optimal for East Asia. The region lies within the mid-latitude westerly belt, where strong anthropogenic emissions are transported eastward over adjacent oceans, making ocean soundings particularly informative for constraining continental outflow signals. Moreover, glint-mode retrievals over the ocean can exhibit precision comparable to, and under certain conditions even higher than, land retrievals owing to more homogeneous surface reflectance conditions (Worden et al., 2017). In this study, we therefore retain both land and ocean soundings and incorporate their reported retrieval uncertainties into the weighting through the observation error covariance matrix, rather than excluding ocean soundings.

In contrast to previous global inversion systems, the present study employs a regional nested inversion framework over East Asia, enabling higher-resolution meteorological fields and improved representation of regional transport processes. Such a configuration is particularly important in East Asia, where strong emission gradients and complex circulation patterns can amplify transport representation errors in coarse-resolution global inversions. In addition, we explicitly account for prior uncertainties in both terrestrial and oceanic fluxes using data-informed estimates from multi-model ensembles. Terrestrial uncertainties are derived from the standard deviation of the TRENDY ensemble (Sitch et al., 2015), while ocean flux uncertainties are based on the standard deviation among ocean models contributing to the Global Carbon Project (Friedlingstein et al., 2023), rather than prescribing fixed percentage values. We further incorporate both land and ocean GOSAT soundings as observational constraints through uncertainty-based weighting, thereby maximizing observational coverage while accounting for retrieval-specific errors. These methodological features provide a more regionally consistent and physically constrained estimate of East Asian NEE, strengthening the robustness of the inferred carbon fluxes. Such refinements support evidence-based policymaking and climate-mitigation strategies.

2 Data and methods

2.1 Observations

GOSAT is a greenhouse gas observation satellite launched in February 2009, operating in a sun-synchronous orbit. Compared to OCO-2, which was launched in 2015, GOSAT has a longer period of available data, making it commonly used in top-down emission estimation studies (Jiang et al., 2022; Byrne et al., 2019; Liu et al., 2021; Houweling et al., 2015). GOSAT provides column-averaged dry-air mole fractions of CO_2, referred to as XCO_2.

We use the Atmospheric CO_2 Observations from Space (ACOS) Version 9.0 Level 2 Lite product (Taylor et al., 2022), covering the period from January 2010 to December 2019 (hereafter GOSAT/ACOS v9). This dataset includes bias correction, with a global mean bias of less than 0.2 ppm (Taylor et al., 2022). It has a spatial resolution of 10.5 km × 10.5 km at nadir and is regridded to 2° × 2.5° (Global) or 0.5° × 0.625° (East Asia) to match model resolutions. To ensure data reliability, only retrievals with a "good" quality flag (0) were used.

We used independent ground-based observations to validate our top-down estimates of CO_2 fluxes. These include data from the World Data Centre for Greenhouse Gases (WDCGG), operated by the Japan Meteorological Agency (JMA) under the Global Atmosphere Watch (GAW) program of the World Meteorological Organization (WMO), which provides

high-precision CO_2 concentration measurements from ground-based stations worldwide. These observations undergo rigorous calibration and quality control procedures, making them highly suitable as an independent benchmark for evaluating model performance. Within the study domain (18.5°N–54°N, 73°E–146°E), a total of eight WDCGG stations with sufficient temporal coverage were identified after applying the RMSE-based filtering criterion described in Section 3. The locations of the WDCGG stations are shown in Figure 1 (red triangles).

Total Carbon Column Observing Network (TCCON; Wunch et al., 2011) provides ground-based measurements of column-averaged CO_2 concentrations (XCO_2) using Fourier transform spectrometers. In this study, we used the GGG2020 product, which includes a priori CO_2 vertical profiles necessary for generating simulated XCO_2 from atmospheric transport models. Within the spatial domain of this study and over the relevant time period, three TCCON sites were available for evaluation. The locations of the TCCON stations are shown in Figure 1 (blue stars).

To aid the interpretation of variability in inferred terrestrial carbon flux, we used the Enhanced Vegetation Index (EVI) as an ancillary satellite-based indicator of vegetation activity. EVI is derived from MODIS surface reflectance and was designed to improve sensitivity in high-biomass regions while reducing canopy-background and atmospheric effects (Huete et al., 2002; Didan and Barreto-Muñoz, 2019). In the MODIS algorithm, EVI is defined as

$$EVI = G\frac{\rho_{NIR}-\rho_{red}}{\rho_{NIR}+C_1\rho_{red}-C_2\rho_{blue}+L} \quad (1)$$

, where ρ_{NIR}, ρ_{red}, and ρ_{blue} denote the near-infrared, red, and blue surface reflectances, respectively; L is the canopy background adjustment term; C_1 and C_2 are aerosol-resistance coefficients; and G is a gain factor. For the standard MODIS EVI product, $L = 1$, $C_1 = 6$, $C_2 = 7.5$, and $G = 2.5$ (Didan and Barreto-Muñoz, 2019). In this study, we used monthly EVI data from MOD13C2, the MODIS Collection 6.1 monthly climate modeling grid product, which provides global vegetation index fields at 0.05° spatial resolution (Didan, 2021).

2.2 Model description

2.2.1 Forward model

We used GEOS-Chem v13.1.0 as a forward model to relate atmospheric CO_2 concentrations to surface fluxes for optimization in the inverse modeling framework. GEOS-Chem is a global 3D chemical transport model driven by meteorological inputs from the Goddard Earth Observing System (GEOS) of NASA's Global Modeling and Assimilation Office (GMAO). The CO_2 simulation in GEOS-Chem was originally developed by Suntharalingam et al. (2004) and later updated by Nassar et al. (2010, 2013). For high-resolution CO_2 simulations over East Asia, we used the nested-grid version of GEOS-Chem driven by Modern-Era Retrospective Analysis for Research and Applications, Version 2 (MERRA-2; Gelaro et al., 2017) meteorological reanalysis data. MERRA-2 provides assimilated meteorological fields at 0.5° × 0.625° horizontal resolution, with variables available at hourly and 3-hourly temporal intervals depending on the data stream. MERRA-2

meteorological fields were used consistently for both the spin-up (2005–2009) and inversion (2010–2019) periods. The global simulation was conducted at 2° × 2.5° horizontal resolution, while the nested East Asia simulation was performed at the same 0.5° × 0.625° resolution as the MERRA-2 fields, with 47 vertical levels extending from the surface to 0.01 hPa. The simulation domain covers East Asia (18.5°N–54°N, 73°E–146°E). Boundary conditions for the nested simulation were taken from global 2° × 2.5° CO_2 fields, which were first constrained by a global inversion using the same inversion framework and GOSAT XCO_2 retrieval product as in this study. Both simulations also shared the same prior flux inventories. This approach helps reduce potential biases in background concentrations entering the nested domain.

We used monthly anthropogenic CO_2 emissions from the Open-source Data Inventory for Anthropogenic CO_2 (ODIAC2020b; Oda and Maksyutov, 2011; Oda et al., 2018) and weekly biomass burning emissions derived from the Global Fire Emissions Database version 4.1 (GFEDv4; Randerson et al., 2018) with CO_2 emissions from shipping and aviation, as well as chemical production from the oxidation of carbon monoxide (CO), methane (CH_4), and non-methane volatile organic compounds (NMVOCs). The model simulates CO_2 sinks as a first-order process using monthly NEE from the Dynamic Land Ecosystem Model (DLEM; Tian et al., 2010; You et al., 2022) and monthly ocean CO_2 fluxes from the Finite-Element Sea ice–Ocean Model coupled with the Regulated Ecosystem Model (FESOM-REcoM; Schourup-Kristensen et al., 2018). The spin-up simulation was performed from 2005 to 2009 without any observational constraint. At the beginning of each annual inversion, the initial 3D CO_2 field was adjusted to ensure that the domain-mean model concentration matched the domain-mean GOSAT XCO_2, following the method of Patra et al. (2021). Independent inversions were then performed for each year from 2010 to 2019.

Our study focused on optimizing NEE and ocean exchange fluxes. Following a common practice in inverse modeling, fossil fuel and biomass burning emissions were prescribed without optimization (e.g., Chevallier et al., 2019; Gurney et al., 2002; Peters et al., 2007). To optimize fluxes consistent with administrative boundaries, we performed tagged-CO_2 simulations that enabled us to independently track CO_2 originating from each region (Figure 1). These defined regions comprise the Korean Peninsula, China, Mongolia, Taiwan, Japan, and parts of the Northwest Pacific.

The averaging kernel, pressure weighting function, and a priori profile from GOSAT/ACOS v9 are used to construct the transformed model XCO_2, incorporating observational sensitivity as defined in Eq. (2) (Connor et al., 2008). This transformation ensures a consistent comparison between the simulated and GOSAT XCO_2.

$$XCO_2^m = XCO_2^a + \sum_j h_j \, a_{CO_2,j} (x_m - x_a)_j \quad (2)$$

Here, XCO_2^m is the transformed model XCO_2, and XCO_2^a is the a priori XCO_2 from GOSAT/ACOS v9. h_j is the pressure weighting function, and $a_{CO_2,j}$ is the corresponding column averaging kernel. x_m represents the simulated vertical CO_2 profile, and x_a is the a priori CO_2 profile from GOSAT/ACOS v9.

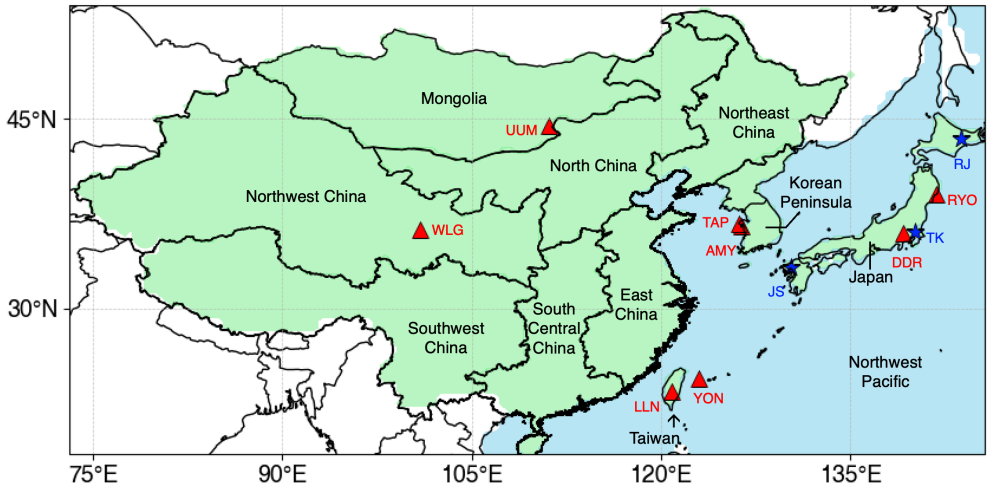

Figure 1. Spatial domains defined in this study for regional analysis over East Asia (18.5°N–54°N, 73°E–146°E), including Mongolia, China (six subregions), the Korean Peninsula, Japan, Taiwan, and the Northwest Pacific. Red triangles indicate surface CO_2 observation sites from the WDCGG network, and blue stars represent TCCON stations.

2.2.2 Inverse model

To infer surface fluxes from atmospheric CO_2 concentrations, we employ an inverse modeling framework based on optimal estimation theory (Rodgers, 2000). Observed concentrations of CO_2, assembled into an observation vector y, are related to the sources and sinks of CO_2 (assembled in a state vector x) through the Jacobian matrix **K**, as described by the following equation:

$$y = Kx + \varepsilon \tag{3}$$

The Jacobian matrix **K** represents the forward model introduced in the previous section. Under the linear approximation, it links variations in the state vector to corresponding changes in the simulated concentrations. The state vector x represents the annual sink/source originating from terrestrial ecosystems and the ocean, while the observation vector y is defined by GOSAT XCO_2 (Sect. 2.1). The error vector ε includes contributions from measurement accuracy, representation error, and errors in model parameters. Here, model parameters refer to all model variables that are not optimized in the inversion. The characteristics of these errors are described by the observation error covariance (S_o), which is represented as the sum of the covariance matrices from individual sources of error.

The fundamental principle of an optimal estimation inverse method is to minimize a cost function $J(x)$:

$$J(x) = (y - Kx)^T S_o^{-1}(y - Kx) + (x - x_a)^T S_a^{-1}(x - x_a) \quad (4)$$

where x_a is the a priori state vector and S_a is the error covariance matrix for the a priori state vector (x_a). The a priori error covariance matrix (S_a) is constructed with the squares of the a priori uncertainties (σ_a^2) as its diagonal elements.

The optimized a posteriori state vector ($\hat{x}$) is given as follows:

$$\hat{x} = x_a + (K^T S_o^{-1} K + S_a)^{-1} K^T S_o^{-1}(y - Kx_a) \quad (5)$$

The superscript **T** indicates the matrix transpose. The a posteriori error covariance matrix $\hat{S}$, which describes the uncertainty of the optimized state estimate, is given by the following expression.

$$\hat{S} = (K^T S_o^{-1} K + S_a^{-1})^{-1} \quad (6)$$

Analogous to the construction of S_a, the diagonal elements of the posterior error covariance matrix $\hat{S}$ correspond to the squared posterior uncertainties ($\hat{\sigma}$). The decrease from prior to posterior uncertainty reflects the degree to which the observations constrain the flux estimates. Accordingly, the uncertainty reduction indicates how much the prior uncertainty is reduced after applying the GOSAT observational constraints.

2.3 Error specification

2.3.1 A priori error covariance (S_a)

The a priori error covariance matrix (S_a) is constructed with the squares of the a priori uncertainties (σ_a) as its diagonal elements. In this study, the σ_a values for terrestrial fluxes are derived from the standard deviation of NEE across eight land models (CABLE-POP, CARDAMOM, CLASSIC, DLEM, EDv3, IBIS, OCN, and YIBS) participating in the Trends in Net Land-Atmosphere Carbon Exchange (TRENDY) project (Sitch et al., 2008). TRENDY is an ensemble of terrestrial biosphere models forced by common meteorological inputs. Similarly, the σ_a values for ocean fluxes are defined using the standard deviation from a ten-model ocean ensemble (ACCESS, CESM, CNRM, FESOM, IPSL, MOM, MPIOM, MRI, NEMO, and NORESM) contributing to the Global Carbon Budget project (Friedlingstein et al., 2023). For each region and each year, annual total fluxes were first calculated separately for each model by spatially integrating the model fluxes over the region, and σ_a was defined as the ensemble standard deviation of these regional annual total fluxes. The resulting annual σ_a values for each region are summarized in Table 1. Note that this mean was computed by averaging the σ_a values directly, not by averaging the variances and then taking the square root.

Only a few previous inversion studies have implemented time-varying prior uncertainties at seasonal or monthly scales (e.g., Baker et al., 2006). Allowing σ_a to vary interannually provides a more consistent representation of how flux uncertainty evolves in response to climate variability. This configuration enables the inversion to account for year-to-year changes in terrestrial and oceanic fluxes, rather than relying on a stationary error structure. In our sensitivity test, time-invariant uncertainties produced regional flux differences that averaged about 12.4% relative to the time-varying case. While this sensitivity analysis does not by itself demonstrate that the time-varying configuration is more realistic, it indicates that allowing σ_a to vary in time can have a non-negligible influence on the inferred regional fluxes.

Table 1. Annual a priori uncertainty (σ_a) for regional fluxes (TgC yr^{-1}). The values are derived from the standard deviation across TRENDY biosphere models (Sitch et al., 2008), except for the Northwest Pacific region, which is estimated from the ocean model ensemble contributing to the Global Carbon Budget (Friedlingstein et al., 2023).

Year	Korean peninsula	Japan	North China	North east China	East China	South Central China	South west China	North west China	Mongolia	Taiwan	North west Pacific
2010	8.7	13.0	22.8	30.1	43.7	38.6	52.1	16.5	12.4	1.3	33.0
2011	6.8	10.2	23.7	17.2	36.3	51.2	34.7	15.0	13.9	1.1	30.8
2012	10.3	10.3	35.7	23.5	35.8	33.4	46.3	14.3	32.1	1.3	31.9
2013	8.7	7.9	32.2	18.1	34.8	28.9	46.8	22.4	36.7	1.1	31.5
2014	9.2	8.3	28.1	21.0	38.0	31.8	28.3	12.6	26.9	1.0	31.6
2015	8.6	12.4	28.2	23.7	37.1	35.4	30.2	23.4	29.1	1.2	27.4
2016	6.0	9.2	31.1	26.7	45.3	36.4	29.6	31.6	15.5	0.9	26.0
2017	9.1	6.5	36.2	31.8	34.5	23.0	23.1	19.0	18.5	1.0	30.4
2018	5.8	14.9	29.7	24.1	40.4	36.9	33.9	18.0	29.6	1.3	30.9
2019	5.4	8.7	31.3	19.4	55.4	48.2	45.7	16.0	25.8	1.3	27.4
Mean	7.8	10.1	29.9	23.6	40.1	36.4	37.1	18.9	24.0	1.2	30.1

2.3.2 Observational error covariance (S_o)

The total observation error covariance, S_o includes contributions from forward model (CTM) error, representation error, and instrument error ($S_o = S_M + S_R + S_I$). The forward model errors are estimated from the relative residual standard deviation (RRSD) of the difference between the model and observation, as represented by ($\mathbf{K}x-y$)/y (Palmer et al., 2003). It is assumed that the mean model bias arises from errors in the a priori sources, and that the variance reflects uncertainty associated with the model. Representation errors are assigned as 1% of the observed concentration (approximately 4 ppm), consistent

with the magnitude reported in previous studies. Kaminski et al. (2010) used an ad hoc variability of 3 ppm, Gerbig et al. (2003) reported representation errors of similar magnitude (~3 ppm), and Tolk et al. (2008) recommended values of around 3 ppm depending on model resolution. The instrument errors are represented using the reported XCO_2 uncertainty provided in the GOSAT/ACOS v9 Level 2 Lite product (Taylor et al., 2022). This per-sounding uncertainty, with a typical magnitude of approximately 1 ppm, varies depending on observing conditions such as signal-to-noise ratio, solar zenith angle, and residual contamination by optically thin clouds or aerosols not fully removed during quality screening (O'Dell et al., 2012; Taylor et al., 2022).

3 Inversion evaluation

To evaluate the reliability of the inversion results, we compared the simulated CO_2 concentrations using the prior and posterior fluxes with independent observational datasets, namely WDCGG and TCCON, which were not assimilated into the inversion system (Feng et al., 2020; Jiang et al., 2021; Jin et al., 2018; Wang et al., 2019). This approach allows for an objective assessment of the inversion performance. Three statistical metrics were employed for the evaluation: correlation coefficient (R), root mean square error (RMSE), and normalized mean bias (NMB), which quantify the linear relationship, overall error magnitude, and systematic bias between the simulated and observed CO_2 concentrations, respectively.

To ensure that the evaluation reflects large-scale, well-mixed CO_2 variability rather than local influences or large representation errors, sites with model–observation RMSE exceeding 7.0 ppm were excluded. This threshold approximately corresponds to the annual amplitude of the seasonal cycle at Mauna Loa, a globally representative background site (Lan et al., 2025). Errors exceeding this threshold suggest that the station is influenced by sub-grid variability that GEOS-Chem cannot resolve at its native resolution, making such sites unsuitable for model evaluation. Following the approach of Jiang et al. (2022), which excluded sites with inadequate model performance, we removed three WDCGG stations (KIS, HKG, and HKO), representing Kisai (Japan), Hong Kong Hok Tsui (China), and Hong Kong King's Park (China). All TCCON stations met the performance criterion and were retained.

We analyzed the inversion results at eight WDCGG and three TCCON observation sites (Sect. 2.1). Since WDCGG provides point-based ground-level measurements, we selected the nearest model grid cell to each observation site based on latitude, longitude, and altitude for comparison. Among the WDCGG sites, all except YON showed improvements in all three statistical metrics, correlation coefficient (R), root mean square error (RMSE), and normalized mean bias (NMB), after the inversion (Table 2). The YON site, located at the southernmost edge of the domain, lies on a small island (~28.9 km^2), which likely introduced substantial representation errors due to the mismatch with the coarser model resolution. For the TCCON observations, which represent column-averaged CO_2 concentrations, we computed the simulated XCO_2 using Eq. (2) to ensure a consistent comparison. All three TCCON sites showed improvements across all evaluation metrics.

The posterior simulation improved the overall model performance, reducing the mean RMSE from 3.08 to 2.94 ppm and the mean NMB from 0.33 % to 0.28 %, while maintaining a high correlation (R = 0.95). Although the overall improvements were moderate, they represent consistent enhancements at 10 of the 11 sites and are statistically significant. A paired t-test across all WDCGG and TCCON sites confirmed significant improvements after the inversion: the correlation coefficient increased ($\Delta R = +0.005$, $p = 0.012$), the normalized mean bias decreased ($\Delta NMB = -0.03$ %, $p = 0.037$), and the RMSE decreased by 0.15 ppm on average ($p = 0.006$). Furthermore, both overestimations (positive NMB at most sites) and underestimations (negative NMB at LLN and TAP) were reduced after optimization, suggesting that the improvement was not coincidental but systematic. A moderate level of improvement, which is commonly reported in CO_2 inversion studies, arises because CO_2 fields are already well constrained by the background state, while the remaining discrepancies are primarily attributed to transport and representation errors. For instance, Kou et al. (2023) reported only marginal improvements (RMSE: 2.65 → 2.63 ppm; R: 0.66 → 0.66; MAE: 2.03 → 2.02 ppm), emphasizing that such modest statistical changes are typical in atmospheric CO_2 inversions.

Table 2. Evaluation metrics for prior and posterior CO_2 concentrations using ground-based observations

Observation	R		NMB (%)		RMSE (ppm)	
	Prior	Posterior	Prior	Posterior	Prior	Posterior
WDCGG						
AMY	0.95	0.95	1.27	1.21	5.87	5.54
DDR	0.95	0.96	0.57	0.51	0.57	0.51
LLN	0.97	0.97	-0.34	-0.33	3.01	2.99
RYO	0.95	0.96	0.49	0.43	3.31	3.03
TAP	0.92	0.93	-0.85	-0.79	4.85	4.59
UUM	0.92	0.93	0.35	0.28	3.61	3.41
WLG	0.95	0.96	0.26	0.18	2.6	2.29
YON	0.99	0.99	0.11	0.13	1.1	1.22
TCCON						
JS	0.97	0.97	0.44	0.43	2.34	2.26
RJ	0.92	0.92	0.70	0.70	3.58	3.56
TK	0.93	0.93	0.61	0.59	2.99	2.87

The spatial distributions of prior and posterior uncertainties are shown in Figure S1. Posterior uncertainties are generally reduced relative to the prior uncertainties across most regions, although the magnitude of reduction varies spatially depending on observational coverage and regional flux sensitivity. To quantify this improvement, we calculate the uncertainty

reduction (UR), a key metric for evaluating inverse-modeling performance that measures the reduction in prior uncertainty (Deng et al., 2007).

The mean UR values for each region during 2010–2019 are summarized in Table 3. The UR in China is relatively high, likely due to its large spatial extent, which allows for the inclusion of more GOSAT XCO_2 pixels, thereby indicating stronger observational constraints. In contrast, Taiwan, due to its much smaller spatial extent, includes relatively fewer GOSAT XCO_2 pixels, resulting in weaker constraints. The UR of regional carbon flux estimates varies substantially across time and space (Deng et al., 2014; Takagi et al., 2011). Over ocean regions, the UR is lower than over land, primarily due to the limited spatial coverage of GOSAT over the ocean. In addition, ocean fluxes are generally much smaller than land fluxes at the grid scale, resulting in a weaker contribution to XCO_2 variability and making them more difficult to constrain using satellite observations. This spatial pattern is consistent with the findings of Deng et al. (2014), who demonstrated that UR is closely related to the spatial coverage of GOSAT XCO_2 observations. While seasonal differences in observational coverage are relatively small, observations are denser over land and more limited over the ocean (Figure S2). Similarly, Jiang et al. (2021) reported that UR over land ranged from 5.9% to 27.2%, whereas ocean UR remained relatively low, ranging from 0.12% to 3.7%. Such large spatial variations in UR highlight its strong dependence on observational density. These results suggest that dense and spatially extensive observational coverage is essential for achieving tighter constraints on regional carbon fluxes.

Table 3. Mean uncertainty reduction rate (UR) for each region for the period 2010-2019

Region	UR (%)
Korean peninsula	3.80
Japan	8.91
North China	41.14
Northeast China	57.02
East China	35.50
South Central China	36.36
Southwest China	28.84
Northwest China	20.74
Mongolia	21.67
Taiwan	0.00
Northwest Pacific	0.66

4 Regional a posteriori CO_2 flux and its annual variability

This section describes regional changes in prior and posterior estimates of carbon fluxes. The 10-year mean NEE increased from –0.17 ± 0.08 PgC yr^{-1} to –0.31 ± 0.06 PgC yr^{-1} (mean ± interannual standard deviation) (Figure 2a, b), while oceanic uptake showed a slight increase from –0.20 ± 0.03 PgC yr^{-1} to –0.21 ± 0.03 PgC yr^{-1}, although this change lies within the range of prior uncertainty and is therefore not statistically significant (Figure 2a, b). Most regions exhibited a trend toward enhanced carbon uptake, as shown in the difference map (Figure 2c).

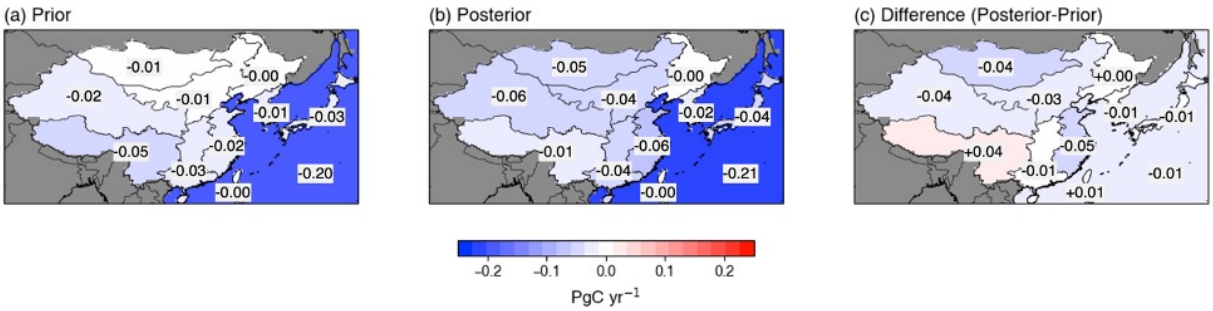

Figure 2. Regional carbon fluxes over East Asia averaged for the period 2010–2019 from (a) the prior estimate, (b) the posterior estimate, and (c) their difference (posterior − prior). Negative values indicate net carbon uptake (sink), and positive values indicate net carbon emissions (source).

In particular, Mongolia, characterized by its vast grasslands, initially showed very weak carbon uptake of –0.01 PgC yr^{-1} in the prior estimate, which increased to –0.05 PgC yr^{-1} in the posterior. Most regions in China experienced increases in carbon uptake, although the magnitude of enhancement varied across subregions. In contrast, carbon uptake weakened in Southwest China, while Northeast China remained nearly neutral with little change from the prior estimate. On the Korean Peninsula, carbon uptake increased, and Japan exhibited a similar level of enhancement. Taiwan, however, showed little to no change. Oceanic regions showed no substantial change.

To help interpret the inferred carbon flux variability, we examine vegetation activity using the Enhanced Vegetation Index (EVI), a widely used satellite-based proxy for photosynthesis. Terrestrial carbon uptake responds non-linearly to complex environmental drivers such as drought and El Niño events (Yue et al., 2017). As a result, vegetation indices cannot perfectly represent variations in carbon fluxes. Despite these limitations, carbon uptake remains fundamentally linked to photosynthetic activity, and EVI provides one of the most practical and widely used proxies for vegetation activity by reflecting vegetation greenness. Noumonvi and Ferlan (2020) also demonstrated that EVI serves as one of the best satellite-based indicators of NEE, even though it cannot fully capture respiration-related processes or short-term environmental stress.

Previous studies (e.g., Wang et al., 2020; Jiang et al., 2021) have used satellite-derived vegetation indices such as EVI, NDVI, and LAI to estimate carbon fluxes. These analyses were generally conducted at coarse spatial scales, typically at continental or subcontinental levels, without resolving fine-scale regional heterogeneity. Following this approach, our comparison also focuses on the domain-averaged behavior. Figure 3 presents the time series of domain-averaged EVI with seasonal variations removed. This increasing trend in EVI suggests enhanced vegetation activity, supporting our finding of increased carbon uptake across most regions of East Asia. Similarly, Wang et al. (2020) attributed China's substantial carbon uptake to the annual rise in vegetation indices.

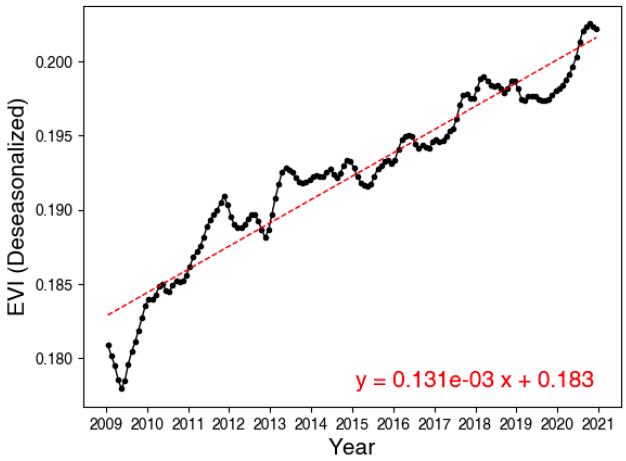

Figure 3. Time series of the domain-averaged Enhanced Vegetation Index (EVI) after removing seasonality. The red dashed line indicates the linear trend fitted to the deseasonalized EVI values.

We examine regional interannual variability and associated supporting evidence, such as El Niño–Southern Oscillation (ENSO) and EVI, that may help explain observed flux patterns. Notably, 2015–2016 coincided with one of the three strongest Super El Niño events on record (1982–83, 1997–98, and 2015–16; Ren et al., 2017; WMO, 2017). ENSO is known to influence photosynthesis and carbon uptake by altering temperature and precipitation patterns (Cox et al., 2013; Fang et al., 2017; Wang et al., 2013; Wang et al., 2014). Accordingly, we focus on ENSO-related impacts and extend the analysis of EVI by conducting correlation analyses to assess its temporal relationship with fluxes.

Figure 4 presents annual CO_2 fluxes for all regions considered in this study over 2010–2019, allowing for direct comparison of prior and posterior estimates across East Asia. The Korean Peninsula acted as a weak carbon sink with low interannual variability. For all years, posterior estimates consistently showed stronger uptake than prior estimates. Japan exhibited a similar pattern, with posterior values exceeding prior ones, and overall low variability. In Mongolia, prior estimates indicated a weak sink, while posterior estimates showed markedly enhanced uptake. Except for 2017, which showed a shift

toward a weak source, all years suggested a sink. In Taiwan, posterior fluxes were comparable to or slightly lower than the prior, and overall fluxes remained relatively stable.

During 2015–2016, reduced carbon uptake was observed in several regions across East Asia, coinciding with the Super El Niño. Bastos et al. (2018) reported that this event substantially reduced terrestrial carbon uptake globally by suppressing ecosystem productivity. Within our study domain, ENSO-related climate anomalies were particularly evident over China, where several studies (Ma et al., 2018; Zhai et al., 2016) consistently reported a characteristic south-flood north-drought pattern.

In northern China (North, Northwest, and Northeast China), precipitation deficits prevailed during the 2015 El Niño peak, especially in North China, where severe summer droughts were reported (Zhai et al., 2016), followed by near-normal or slightly wetter conditions in 2016 (Ma et al., 2018). These anomalies are consistent with our results, which indicate a transition from carbon release in 2015 (0.008 PgC yr^{-1}) to weak carbon uptake in 2016 (−0.005 PgC yr^{-1}; Figure 4). In Northwest China, by contrast, the residual effects of the 2015–2016 El Niño brought unusually high rainfall during 2016 (Lu et al., 2019), particularly in spring and autumn, when precipitation exceeded 150% of the climatological mean (Ma et al., 2018). As noted by Liu et al. (2024), vegetation in arid regions tends to respond positively to increased moisture availability, and our posterior flux estimates indeed indicate sustained or even enhanced carbon uptake during this period. Specifically, the mean flux during 2015–2016 (−0.078 PgC yr^{-1}) was more negative than the decadal mean excluding those years (−0.054 PgC yr^{-1}), suggesting strengthened carbon uptake under wetter conditions. In Northeast China, interannual flux variability was large, with strong uptake in 2016, but the statistical correlation with ENSO remained insignificant ($p > 0.05$; Ma et al., 2018). This region encompasses diverse vegetation types and spans arid to humid zones (see Jiang et al., 2022; Fig. 1b), potentially explaining its high interannual flux variability.

In southern China (East, South Central, and Southwest China), the El Niño–induced precipitation anomalies were generally opposite to those in the northern China. Southwest China represented an exception. While East and South Central China experienced excessive rainfall and flooding, Southwest China underwent persistent drought due to weakened southward moisture transport (Ma et al., 2018). This region suffered from prolonged drought conditions from summer 2015 through spring 2016, leading to vegetation water stress and reduced carbon uptake, with net carbon emissions of 0.011 and 0.023 PgC yr^{-1} during these two years. This drought-induced water limitation likely explains the reduced carbon uptake observed over Southwest China during 2015–2016. In contrast, the summer 2016 flood in East China was particularly severe. The WMO reported that flooding across the Yangtze River Basin in summer 2016 was the most serious since 1999 (WMO, 2017). This extreme rainfall event coincided with a marked shift toward positive NEE (+0.092; carbon release) in 2016 (Figure 4). South Central China similarly exhibited enhanced precipitation and frequent flooding during 2015–2016 (Ma et al., 2018), corresponding to nearly neutral and carbon-releasing conditions in those years (−0.001 and +0.011 PgC yr^{-1}).

While numerous studies have addressed the effects of ENSO on temperature, precipitation, and extreme weather events, few have explored its direct influence on regional carbon fluxes. When comparing the temporal patterns of precipitation (ERA5; Hersbach et al., 2020) and carbon flux anomalies, a statistically significant time-series correlation is difficult to identify.

This is likely because carbon flux variability is influenced by multiple environmental drivers beyond precipitation alone (e.g., temperature and radiation), as well as ecosystem nonlinearity, potential lag effects, and regional climatic heterogeneity. Nevertheless, during the strong 2015–2016 El Niño event, the precipitation anomalies and corresponding flux responses appear qualitatively consistent, providing additional support for our event-based interpretation (Figure S3). Our analysis therefore provides new evidence that ENSO-related climatic variability can influence terrestrial ecosystem carbon uptake across East Asia, helping to bridge this critical research gap.

We also analyzed the correlations between EVI and carbon uptake, defined here as NEP (= −NEE) so that positive values indicate uptake. Overall, the correlations strengthened across most regions (Table 4), particularly in the northern part of the domain, including Northwest China, Korean Peninsula, and Japan. For example, the correlation coefficients increased from 0.60 → 0.75 in Korean Peninsula**,** 0.55 → 0.69 in Japan**,** and 0.09 → 0.78 in Northwest China**,** respectively. In North and Northeast China and Mongolia, the correlations shifted from negative to positive, while East China showed a slight increase.

However, it is unrealistic to expect consistent improvement in vegetation–carbon correlations across all regions. For reference, Jiang et al. (2021) compared the relationships between carbon sinks and two vegetation-related indicators (SDA and LAI; see their Table 5) and reported improvements in correlations in fewer than half of the regions examined. In our study, correlations weakened in South Central and Southwest China, whereas the negative correlation persisted in Taiwan. These southern regions are dominated by evergreen broad-leaved forests (Zhu and Tan, 2024). According to Buchmann and Schulze (1999), broad-leaved forests differ from other ecosystems in that leaf area index (LAI) does not significantly correlate with carbon uptake, due to self-shading and increased ecosystem respiration that offset photosynthetic gains. Although EVI differs from LAI, Potithep et al. (2013) reported a high correlation between the two in broad-leaved forests ($r^2 = 0.96$), suggesting a close relationship. This may explain why EVI–carbon uptake correlations did not improve in South and Southwest China and Taiwan, where broad-leaved forest characteristics dominate.

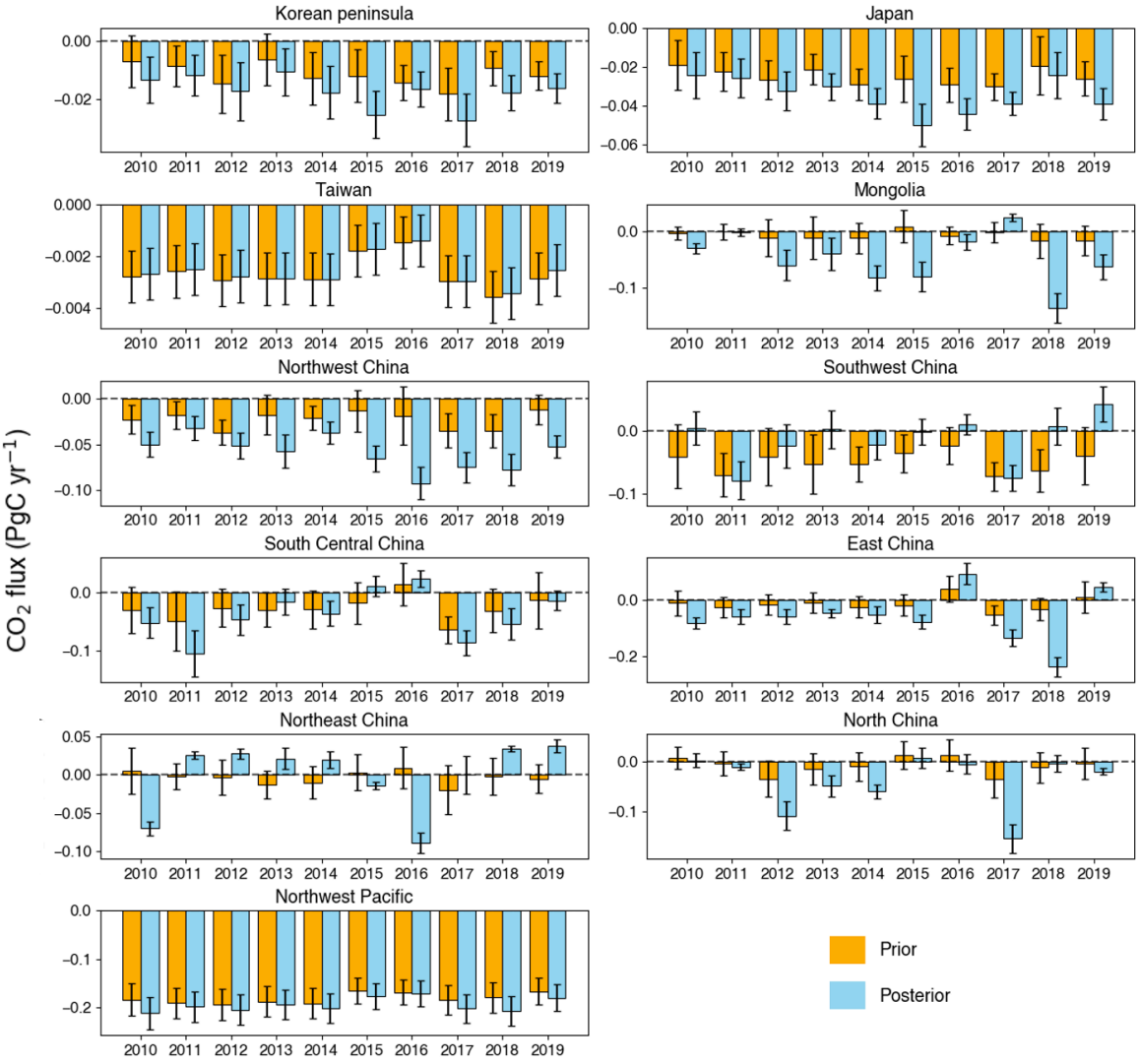

Figure 4. Annual regional CO_2 fluxes over East Asia for the period 2010–2019, estimated from the prior (orange) and posterior (blue) fluxes. Each panel represents a different region, and negative values indicate net CO_2 uptake (sink). Error bars represent the uncertainty of the flux estimates.

Table 4. Correlation coefficients between Enhanced Vegetation Index (EVI) and regional terrestrial ecosystems CO_2 uptake (NEP = −NEE).

Region	Correlation coefficient with EVI	
	Prior	Posterior
Korean peninsula	0.60	0.75
Japan	0.55	0.69
North China	−0.13	0.07
Northeast China	−0.01	0.32
East China	0.04	0.13
South Central China	−0.21	−0.39
Southwest China	−0.03	−0.08
Northwest China	0.09	0.78
Mongolia	−0.13	0.06
Taiwan	−0.24	−0.22

5. Comparison of our top-down estimates with other products

In this study, we examine the characteristics and discrepancies of our posterior carbon flux estimates by comparing them with a suite of established products derived from diverse estimation frameworks. The comparison encompasses FLUXCOM (NEE), GCAS2021 (NEE), TRENDY (NEE), OCO-2 v10 MIP (NEE and ocean), CMS-Flux Ocean v3 (ocean), and the Global Carbon Project ocean ensemble (process-based and observation-based).

The FLUXCOM RS product estimates global terrestrial carbon fluxes by applying multiple machine learning algorithms, including Multivariate Adaptive Regression Splines (MARS), to satellite-based remote sensing inputs (Jung et al., 2020). As the FLUXCOM dataset is available only through 2018, while the other products extend to 2019, the comparison for FLUXCOM is limited to that period. GCAS2021 (Jiang et al., 2022) provides a NEE product derived from GOSAT XCO_2 retrievals using the Global Carbon Assimilation System (GCAS), an inverse modeling framework that shares a satellite-based foundation with this study. The TRENDY (Trends in net land–atmosphere carbon exchange) project is a multi-model ensemble (bottom-up framework) designed to assess long-term trends in global terrestrial carbon fluxes. It integrates multiple Earth system and dynamic global vegetation models driven by common input datasets, including atmospheric CO_2 concentration, meteorological forcing, and land-use changes (Sitch et al., 2008). In this study, we used an ensemble of eight models—CABLE-POP, CARDAMOM, CLASSIC, DLEM, EDv3, IBIS, OCN, and YIBS—all of which simulate the full carbon cycle processes encompassing photosynthesis, respiration, carbon storage, and land-use change.

We further include the OCO-2 v10 Model Intercomparison Project (MIP), specifically the LNLGOGIS inversion configuration, which assimilates OCO-2 XCO_2 retrievals from land nadir, land glint, and ocean glint observations together with in situ measurements (Crowell et al., 2019). The OCO-2 MIP ensemble provides an independent set of atmospheric inversion estimates using multiple transport models and prior flux assumptions, thereby serving as an additional benchmark for evaluating both terrestrial and ocean carbon flux estimates. It should be noted that the OCO-2 v10 MIP provides net biosphere exchange (NBE) rather than net ecosystem exchange (NEE). To ensure consistency with our flux definition, we therefore subtracted fire emissions from the NBE estimates using the GFED4 fire inventory, which is also used in our inversion framework.

For the ocean domain, the CMS-Flux Ocean v3 product (Bowman, 2024) represents a posterior estimate generated under NASA's Carbon Monitoring System (CMS), combining GOSAT and OCO-2 observations with an atmospheric transport model to infer global air–sea CO_2 exchange. In addition, we compare our estimates with ocean flux products from the Global Carbon Budget (GCB; Friedlingstein et al., 2023), which include both process-based Global Ocean Biogeochemistry Models (GOBMs) and observation-based reconstructions derived from surface pCO_2 measurements. The process-based ensemble consists of ten ocean biogeochemical models—ACCESS, CESM, CNRM, FESOM, IPSL, MOM, MPIOM, MRI, NEMO, and NORESM—which simulate large-scale ocean circulation and marine carbon processes governing global air–sea CO_2 exchange. The observation-based ensemble reconstructs air–sea CO_2 fluxes using surface pCO_2 measurements and statistical or machine-learning interpolation approaches. In this study, we use eight observation-based products: CMEMS-LSCE-FFNN, CSIR-ML6, JENA-MLS, LDEO-HPD, NIES-ML3, OceanSODA-ETHZv2, UExP-FNN-U, and VLIZ-SOMFFN.

As shown in Figure 5a, our posterior estimates consistently indicate enhanced terrestrial carbon uptake relative to the prior and are comparable to other top-down products (FLUXCOM and GCAS) as well as the bottom-up ensemble (TRENDY). The magnitude of the terrestrial carbon sink inferred in this study (-0.31 PgC yr^{-1}) is broadly consistent with the terrestrial sink estimate reported by Wang et al. (2024) for East Asia during 2000–2019 (-0.27 PgC yr^{-1}; Figure 5).

The posterior results show closer agreement with these datasets than the prior does. However, in 2016, although the posterior estimates remain closer to the other products than the prior, a slight discrepancy persists, likely due to the nearly neutral prior flux that year. Over the ocean, the posterior estimates show a comparable magnitude of carbon uptake to both the prior and alternative products (Figure 5b). Although the posterior mean suggests a marginally stronger sink, the difference lies within the uncertainty range and is therefore not statistically significant. This result remains consistent with the bottom-up ensemble (Global Carbon Budget Ocean).

The ocean remains a region of limited observational coverage, where variability in data availability and input types can lead to differences among products. The Northwest Pacific, our primary ocean focus region, is particularly characterized by complex coastal geometries and sparse surface pCO_2 observations, thereby contributing to elevated uncertainties and product-level discrepancies (Wu et al., 2025). Further contributing factors include differences in observational datasets and model configurations. The CMS-Flux Ocean v3 product assimilates satellite observations from GOSAT v7.3 and OCO-2 within an atmospheric inversion framework. GCAS2021 also uses the GOSAT v9 retrievals employed in this study, but differs

by adopting CT2019B as the prior flux and MOZART-4 as the transport model instead of GEOS-Chem. The OCO-2 v10 MIP estimates used here are based on the LNLGOGIS atmospheric inversion system, which integrates OCO-2 XCO_2 observations from multiple viewing geometries along with in situ CO_2 measurements. In addition, the Global Carbon Budget ocean products include both process-based ocean biogeochemical models and observation-based pCO_2 reconstructions, which rely on different observational constraints and modeling approaches. These methodological differences likely contribute to the discrepancies observed among the flux estimates.

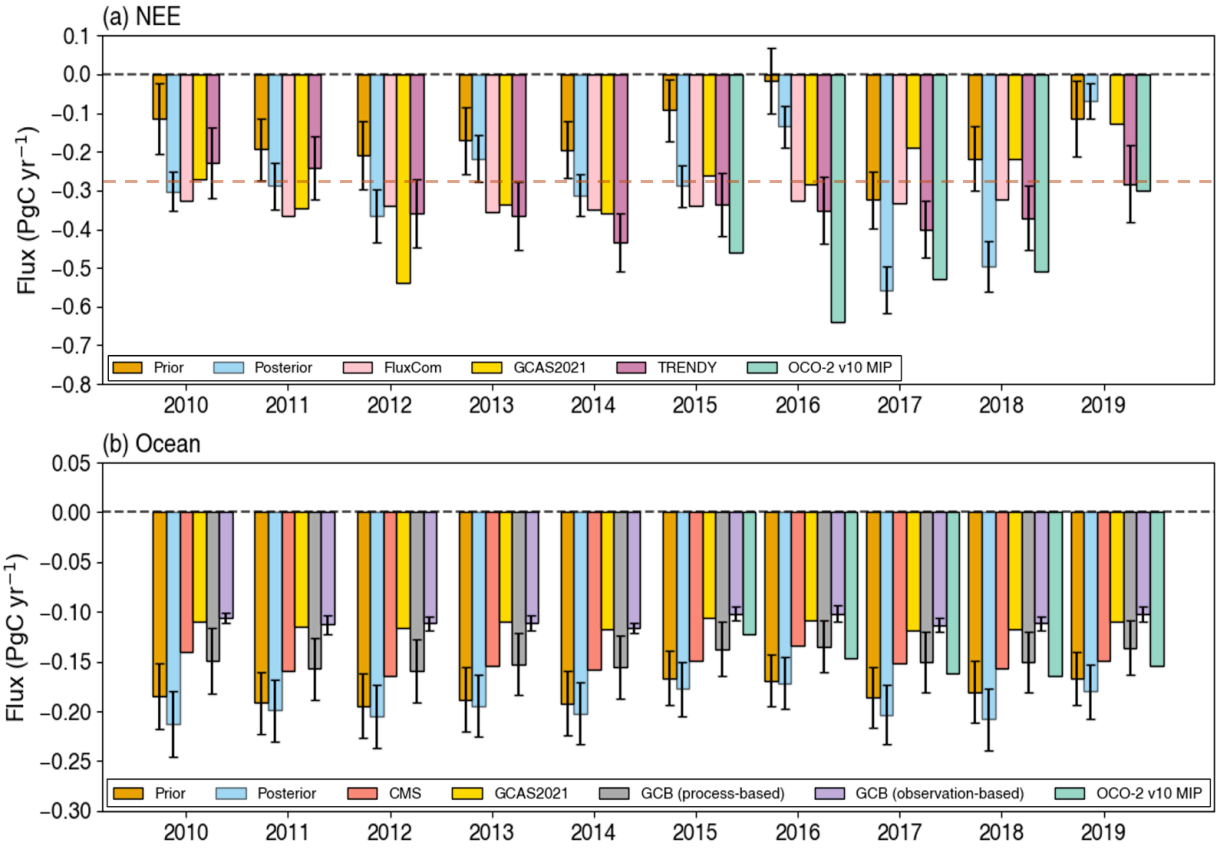

Figure 5. Comparison of prior and posterior flux estimates with other flux products from 2010 to 2019. (a) NEE and (b) Ocean carbon flux over East Asia. Bars indicate annual mean fluxes from each dataset. Error bars represent the uncertainty ranges for the prior and posterior estimates, while those for TRENDY and GCB Ocean denote the inter-model standard deviations. The orange dashed line is the NEE of East Asia for 2000-2020 calculated by RECCAP-2 (Wang et al., 2024)

6 East Asia Carbon Budget (2010–2019)

The carbon budget of East Asia for 2010–2019, incorporating the sink estimated in this study, is summarized as follows (Figure 6; see Appendix A for details of the calculation method). Fossil fuel and biomass burning emissions are derived from ODIAC and GFED4, respectively. Fossil fuel emissions amount to 3.86 PgC yr^{-1}. Compared with the global total fossil fuel emissions of 9.6 PgC yr^{-1} (Friedlingstein, 2020), East Asia accounts for about 40% of the global fossil carbon release.

Biomass burning contributes 0.11 PgC yr^{-1}, while the regional NEE and ocean uptake are −0.31 PgC yr^{-1} and −0.21 PgC yr^{-1}, respectively. These yield a combined sink of −0.52 PgC yr^{-1}, offsetting only 13.6% of fossil fuel emissions. Consequently, the residual carbon that is not compensated by natural sinks accumulates in the atmosphere, leading to an increase in atmospheric CO_2 concentrations. This imbalance between emissions and sinks explains the persistently high atmospheric CO_2 levels observed over East Asia (Yeh et al., 2023). The atmospheric carbon stock over East Asia is estimated at 38.97 PgC, representing the amount of CO_2 currently retained within the regional atmosphere.

In our East Asia domain, the net surface flux (fossil fuel + biomass burning + NEE + ocean uptake, with NEE and ocean uptake typically negative) is +3.45 PgC yr^{-1} for 2010–2019, indicating a strong net source to the atmosphere. Over the same period, the vertically integrated atmospheric carbon mass within the domain increases at a mean rate of ~0.24 PgC yr^{-1}, implying that only about 7% of the emitted carbon remains stored locally in the atmospheric column. The remaining ~3.21 PgC yr^{-1}, ~93% of the net source, is exported out of the domain by large-scale transport. Most of the carbon emitted from East Asia is transported beyond the regional boundaries. Therefore, East Asian emissions are not confined to a local issue but are linked to downstream transport influencing other regions.

Despite gradual increases in NEE and ocean uptake due to fertilization effects and enhanced solubility associated with pCO_2 gradients, East Asia remains dominated by large fossil fuel emissions. Given this limited natural sink capacity, achieving carbon neutrality will require substantial reductions in fossil fuel use and the enhancement of anthropogenic removals, such as carbon capture and storage (CCS).

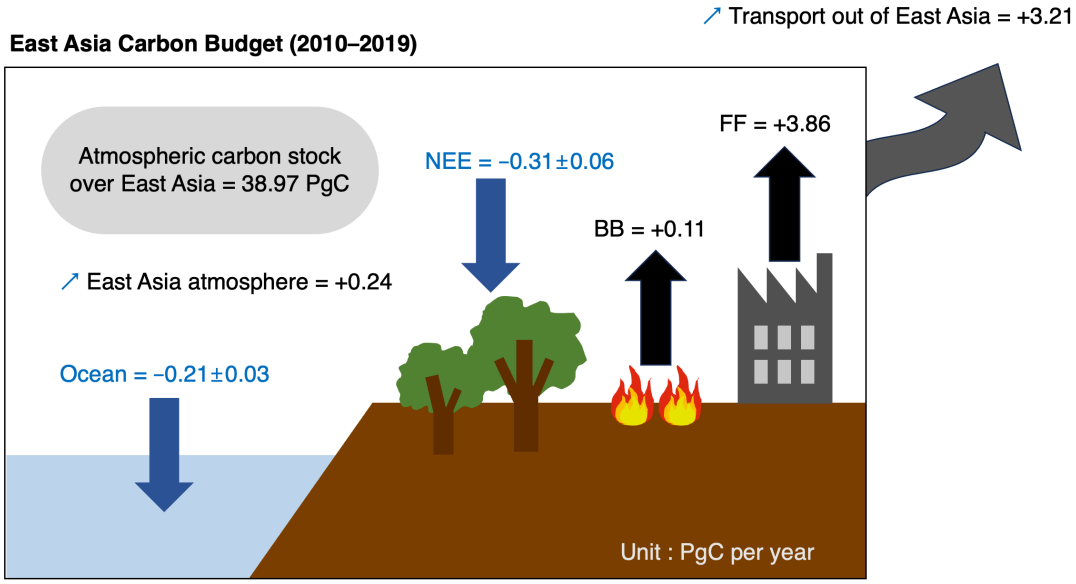

Figure 6. Schematic diagram of the East Asia carbon budget averaged for 2010–2019 (18.5° N–54° N, 73° E–146° E). The atmospheric carbon stock over East Asia, estimated at 38.97 PgC, represents the amount of CO_2 retained within the regional atmosphere. All other fluxes are expressed in PgC yr^{-1} (FF = fossil fuel combustion; BB = biomass burning; NEE = net ecosystem exchange). Downward blue arrows represent CO_2 uptake by the terrestrial and ocean, whereas upward black arrows indicate emissions from biomass burning and fossil fuel combustion.

7. Summary and conclusions

This study provides a top-down estimate of regional carbon fluxes across East Asia (18.5°N–54°N, 73°E–146°E) for the period 2010–2019, using a Bayesian inversion framework constrained by GOSAT ACOS v9 XCO_2 retrievals. By applying the GEOS-Chem chemical transport model and incorporating region-specific prior uncertainties based on the standard deviation of terrestrial and ocean carbon fluxes, we optimized both terrestrial and oceanic fluxes. The posterior estimates indicate enhanced carbon uptake compared to the prior, with mean terrestrial NEE ranging from –0.17 to –0.31 PgC yr^{-1} while oceanic uptake changed slightly from –0.20 to –0.21 PgC yr^{-1}, showing no statistically significant difference.

Evaluation against independent surface-based CO_2 observations (WDCGG and TCCON) showed consistent improvements across most stations in terms of correlation, RMSE, and bias, supporting the robustness of the inversion framework. Uncertainty reduction (UR) was generally more substantial over continental regions such as China, whereas smaller or oceanic regions showed limited improvements due to observational constraints.

At the regional scale, most regions acted as persistent carbon sinks throughout the decade, with interannual variability influenced by climate events. Notably, the 2015–2016 Super El Niño was associated with temporary flux reversals, primarily over several regions in China. These reversals were largely driven by ENSO-induced floods and droughts, which suppressed vegetation photosynthetic activity and, in some regions, led to near-neutral or even positive NEE values, indicating temporary

carbon release. This suggests that terrestrial carbon sinks can be substantially weakened not only by natural climatic variability such as ENSO, but also by extreme weather events intensified under climate change. An increasing trend in the Enhanced Vegetation Index (EVI), along with improved correlations between EVI and posterior carbon uptake, further supports the credibility of the flux estimates. However, regions dominated by broadleaf forests exhibited persistent negative correlations, likely due to self-shading effects of dense canopies.

Comparison with other top-down and bottom-up flux products showed general agreement in both trend and magnitude. Nonetheless, discrepancies remain, largely due to differences in observational inputs, modeling frameworks, and prior flux assumptions. In particular, oceanic uptake estimates tend to diverge more than terrestrial ones, as ocean regions are more sparsely observed and often include complex coastal zones (Wu et al., 2025). In addition, fossil fuel emissions were prescribed and not optimized in this study. Thompson et al. (2016) estimated that uncertainty in the growth rate of these emissions accounted for about 32% of the uncertainty in the inferred East Asian land sink. Given the large magnitude of anthropogenic emissions in East Asia, differences among fossil fuel emission inventories may influence inversion-based estimates of terrestrial carbon fluxes and should therefore be considered when interpreting our results.

Although the optimized posterior fluxes indicate enhanced carbon uptake compared to the prior, the East Asian domain remains highly fossil-fuel-dominant. Approximately 7% of the residual carbon accumulates within the regional atmosphere, while the remaining 93% is transported out of the domain by large-scale circulation. Considering the limited capacity of natural carbon sinks, new strategies will be required to mitigate both the persistently high atmospheric CO_2 concentrations over East Asia and the downstream transport of these emissions to other regions.

Overall, this study estimates carbon sinks over East Asia by incorporating region-specific uncertainties and demonstrates the effective use of satellite constraints and a chemical transport model in inverse modeling. The results were evaluated against independent observations and compared with other flux products, while the interannual variability was interpreted through ENSO and vegetation indices. However, the relatively limited observational coverage over ocean regions resulted in smaller uncertainty reductions, highlighting the need for denser and more continuous oceanic CO_2 observations to further constrain regional flux estimates. Despite this limitation, this study provides valuable insights into the East Asian carbon cycle, which is critical for carbon management, and can support policy strategies aimed at mitigating climate change.

Appendix A : Calculation of the East Asia carbon budget

The carbon budget over East Asia was estimated based on the conservation of carbon mass within the regional atmospheric column. The carbon balance over the domain can be expressed as

$$\frac{dC_{atm}}{dt} = F_{net} - F_{export},$$

where C_{atm} is the atmospheric carbon mass within the East Asia domain, F_{net} is the net surface carbon flux, and F_{export} represents the net lateral carbon transport out of the domain.

The net surface carbon flux was calculated as the sum of fossil fuel emissions (FF), biomass burning emissions (BB), terrestrial net ecosystem exchange (NEE), and ocean–atmosphere carbon flux:

$$F_{net} = F_{\mathrm{FF}} + F_{\mathrm{BB}} + F_{\mathrm{NEE}} + F_{\mathrm{ocean}},$$

where positive values denote carbon release to the atmosphere and negative values represent carbon uptake by land or ocean. Using the mean fluxes during 2010–2019, fossil fuel emissions and biomass burning contributed +3.86 and +0.11 PgC yr^{-1}, respectively, while terrestrial and ocean uptake were −0.31 and −0.21 PgC yr^{-1}. The resulting net surface flux over East Asia is therefore

$$F_{net} = +3.45\ \mathrm{PgC\ yr^{-1}},$$

Atmospheric carbon storage within the East Asia domain was estimated by vertically integrating posterior CO_2 concentrations over the atmospheric column and converting the result to units of PgC. The atmospheric carbon mass can be written as

$$C_{\mathrm{atm}} = \int_V X_{\mathrm{CO_2}}\ \rho_{\mathrm{air}}\ dV,$$

where $X_{\mathrm{CO_2}}$ is the CO_2 dry mole fraction, ρ_{air} is the air density, and V represents the atmospheric volume over the East Asia domain. This integration yields annual atmospheric carbon stock values $C_{\mathrm{atm}}(t)$ for each year during 2010–2019. The mean atmospheric carbon stock during the study period was estimated to be 38.97 PgC.

The temporal change in atmospheric carbon storage was derived from the difference between the 2019 and 2010 carbon stocks:

$$\frac{dC_{\mathrm{atm}}}{dt} = \frac{C_{\mathrm{atm},2019} - C_{\mathrm{atm},2010}}{\Delta t},$$

which corresponds to an average storage increase of approximately

$$\frac{dC_{\mathrm{atm}}}{dt} = 0.24 PgC\ \mathrm{yr}^{-1}.$$

Finally, the net carbon export from the East Asia domain was diagnosed as the residual of the mass balance equation:

$$F_{\mathrm{export}} = F_{net} - \frac{dC_{\mathrm{atm}}}{dt}.$$

Substituting the estimated values yields

$$F_{export} = 3.45 - 0.24 \ = \ +3.21\ PgC\ yr^{-1}.$$

This result indicates that most of the carbon emitted within East Asia is transported out of the region by atmospheric circulation rather than accumulating locally within the atmospheric column.

Data availability

The GOSAT ACOS v9 XCO_2 retrievals are publicly available from the NASA GES DISC (https://disc.gsfc.nasa.gov; Taylor et al., 2022). Ground-based CO_2 observations are available from the World Data Centre for Greenhouse Gases (WDCGG; https://gaw.kishou.go.jp/). The TCCON (Total Carbon Column Observing Network) data used in this study are publicly available at https://tccondata.org/. The MODIS/Terra EVI data (MOD13C2 Version 6.1) were obtained from the NASA Land Processes Distributed Active Archive Center (LP DAAC), USGS/Earth Resources Observation and Science Center (https://lpdaac.usgs.gov/). The TRENDY model simulation result and Ocean flux products from the Global Carbon Budget 2023 are available via the ICOS Carbon Portal as part of the Global Carbon Budget open data. (https://mdosullivan.github.io/GCB/) The GCAS2021 data are available at https://doi.org/10.5281/zenodo.5829774 (Jiang, 2022). The FLUXCOM data are publicly available for download (CC BY 4.0 license) from the Max Planck Institute for

Biogeochemistry (MPI-BGC) data portal after registration (https://www.fluxcom.org). The CMS-Flux Ocean v3 posterior flux product is available from the NASA Goddard Earth Sciences Data and Information Services Center (GES DISC; DOI: 10.5067/9H6GCQKP28AI). The CMEMS-LSCE ocean carbon product is available from the Copernicus Marine Environment Monitoring Service (DOI: 10.48670/moi-00047). The OCO-2 v10 Model Intercomparison Project (MIP) flux products are publicly available from the NOAA Global Monitoring Laboratory (GML) data portal (https://www.gml.noaa.gov/ccgg/OCO2_v10mip/download.php). Monthly precipitation data from the ERA5 reanalysis were obtained from the Copernicus Climate Data Store (CDS; https://cds.climate.copernicus.eu/).

Author contributions

RJP designed the study. MK analyzed the data and wrote the manuscript. JJ supported the data analysis. SIO contributed to the discussion. ESH provided the code used in this study. JIJ and SWY provided valuable comments and advice.

Competing interests

The authors declare that they have no conflict of interest.

Acknowledgements

We acknowledge the data providers of GOSAT, WDCGG, TCCON, TRENDY, Global Carbon Project and other sources used in this study. We thank the developers of the GEOS-Chem model and the global carbon flux products for making their data publicly available.

Financial support

This work was supported by the National Research Foundation of Korea (NRF) grant funded by the Korea government (MSIT) (RS-2021-NR057872 and RS-2024-00353508).

References

Baker, D. F., Law, R. M., Gurney, K. R., Rayner, P., Peylin, P., Denning, A. S., Bousquet, P., Bruhwiler, L., Chen, Y. H., Ciais, P., Fung, I. Y., Heimann, M., John, J., Maki, T., Maksyutov, S., Masarie, K., Prather, M., Pak, B., Taguchi, S., and Zhu, Z.: TransCom 3 inversion intercomparison: Impact of transport model errors on the interannual variability of regional CO2 fluxes, 1988-2003, Global Biogeochem. Cycles, 20, https://doi.org/10.1029/2004GB002439, 2006.

Bastos, A., Friedlingstein, P., Sitch, S., Chen, C., Mialon, A., Wigneron, J. P., Arora, V. K., Briggs, P. R., Canadell, J. G., Ciais, P., Chevallier, F., Cheng, L., Delire, C., Haverd, V., Jain, A. K., Joos, F., Kato, E., Lienert, S., Lombardozzi, D., Melton, J. R., Myneni, R., Nabel, J. E. M. S., Pongratz, J., Poulter, B., Rödenbeck, C., Séférian, R., Tian, H., Van Eck, C., Viovy, N., Vuichard, N., Walker, A. P., Wiltshire, A., Yang, J., Zaehle, S., Zeng, N., and Zhu, D.: Impact of the 2015/2016 El Niño on the terrestrial carbon cycle constrained by bottom-up and top-down approaches, Philosophical Transactions of the Royal Society B: Biological Sciences, 373, https://doi.org/10.1098/rstb.2017.0304, 2018.

Basu, S., Baker, D. F., Chevallier, F., Patra, P. K., Liu, J., and Miller, J. B.: The impact of transport model differences on CO2 surface flux estimates from OCO-2 retrievals of column average CO2, Atmos. Chem. Phys., 18, 7189–7215, https://doi.org/10.5194/acp-18-7189-2018, 2018.

Bowman, K.: Carbon Monitoring System Carbon Flux Ocean Prior L4 V3, Greenbelt, MD, 2024.

Buchmann, N. B. and Schulze, E. D.: Net CO2 and H2O fluxes of terrestrial ecosystems, Global Biogeochem. Cycles, 13, 751–760, https://doi.org/10.1029/1999GB900016, 1999.

Byrne, B., Jones, D. B. A., Strong, K., Polavarapu, S. M., Harper, A. B., Baker, D. F., and Maksyutov, S.: On what scales can GOSAT flux inversions constrain anomalies in terrestrial ecosystems?, Atmos. Chem. Phys., 19, 13017–13035, https://doi.org/10.5194/acp-19-13017-2019, 2019.

Canadell, J. G., Ciais, P., Gurney, K., Le Quéré, C., Piao, S., Raupach, M. R., and Sabine, C. L.: An International Effort to Quantify Regional Carbon Fluxes, Eos, Transactions American Geophysical Union, 92, 81–82, https://doi.org/https://doi.org/10.1029/2011EO100001, 2011.

Chevallier, F., Remaud, M., O'Dell, C. W., Baker, D., Peylin, P., and Cozic, A.: Objective evaluation of surface- and satellite-driven carbon dioxide atmospheric inversions, Atmos. Chem. Phys., 19, 14233–14251, https://doi.org/10.5194/acp-19-14233-2019, 2019.

Connor, B. J., Boesch, H., Toon, G., Sen, B., Miller, C., and Crisp, D.: Orbiting Carbon Observatory: Inverse method and prospective error analysis, Journal of Geophysical Research Atmospheres, 113, https://doi.org/10.1029/2006JD008336, 2008.

Cox, P. M., Pearson, D., Booth, B. B., Friedlingstein, P., Huntingford, C., Jones, C. D., and Luke, C. M.: Sensitivity of tropical carbon to climate change constrained by carbon dioxide variability, Nature, 494, 341–344, https://doi.org/10.1038/nature11882, 2013.

Crowell, S., Baker, D., Schuh, A., Basu, S., Jacobson, A. R., Chevallier, F., Liu, J., Deng, F., Feng, L., McKain, K., Chatterjee, A., Miller, J. B., Stephens, B. B., Eldering, A., Crisp, D., Schimel, D., Nassar, R., O'Dell, C. W., Oda, T., Sweeney, C., Palmer,

P. I., and Jones, D. B. A.: The 2015-2016 carbon cycle as seen from OCO-2 and the global in situ network, Atmos. Chem. Phys., 19, 9797–9831, https://doi.org/10.5194/acp-19-9797-2019, 2019.

Deng, F. and Chen, J. M.: Recent global CO 2 flux inferred from atmospheric CO 2 observations and its regional analyses, Biogeosciences, 8, 3263–3281, https://doi.org/10.5194/bg-8-3263-2011, 2011.

Deng, F., Chen, J. M., Ishizawa, M., Yuen, C. W., Mo, G., Higuchi, K., Chan, D., and Maksyutov, S.: Global monthly CO2 flux inversion with a focus over North America, in: Tellus, Series B: Chemical and Physical Meteorology, 179–190, https://doi.org/10.1111/j.1600-0889.2006.00235.x, 2007.

Deng, F., Jones, D. B. A., Henze, D. K., Bousserez, N., Bowman, K. W., Fisher, J. B., Nassar, R., O'Dell, C., Wunch, D., Wennberg, P. O., Kort, E. A., Wofsy, S. C., Blumenstock, T., Deutscher, N. M., Griffith, D. W. T., Hase, F., Heikkinen, P., Sherlock, V., Strong, K., Sussmann, R., and Warneke, T.: Inferring regional sources and sinks of atmospheric CO2 from GOSAT XCO2 data, Atmos. Chem. Phys., 14, 3703–3727, https://doi.org/10.5194/acp-14-3703-2014, 2014.

Didan, K.: MODIS/Terra Vegetation Indices Monthly L3 Global 0.05Deg CMG V061, NASA Land Processes Distributed Active Archive Center, https://doi.org/https://doi.org/10.5067/MODIS/MOD13C2.061, 2021.

Didan, K. and Barreto-Muñoz, A.: MODIS Vegetation Index User's Guide (MOD13 Series), Version 3.10, Collection 6.1, Vegetation Index and Phenology Lab, University of Arizona, 2019.

Fang, Y., Michalak, A. M., Schwalm, C. R., Huntzinger, D. N., Berry, J. A., Ciais, P., Piao, S., Poulter, B., Fisher, J. B., Cook, R. B., Hayes, D., Huang, M., Ito, A., Jain, A., Lei, H., Lu, C., Mao, J., Parazoo, N. C., Peng, S., Ricciuto, D. M., Shi, X., Tao, B., Tian, H., Wang, W., Wei, Y., and Yang, J.: Global land carbon sink response to temperature and precipitation varies with ENSO phase, Environmental Research Letters, 12, https://doi.org/10.1088/1748-9326/aa6e8e, 2017.

Feng, S., Jiang, F., Wu, Z., Wang, H., Ju, W., and Wang, H.: CO Emissions Inferred From Surface CO Observations Over China in December 2013 and 2017, Journal of Geophysical Research: Atmospheres, 125, https://doi.org/10.1029/2019JD031808, 2020.

Friedlingstein, P.: Global carbon budget 2020, Earth Syst Sci Data, 12, https://doi.org/10.5194/essd-12-3269-2020, 2020.

Friedlingstein, P., O'Sullivan, M., Jones, M. W., Andrew, R. M., Bakker, D. C. E., Hauck, J., Landschützer, P., Le Quéré, C., Luijkx, I. T., Peters, G. P., Peters, W., Pongratz, J., Schwingshackl, C., Sitch, S., Canadell, J. G., Ciais, P., Jackson, R. B., Alin, S. R., Anthoni, P., Barbero, L., Bates, N. R., Becker, M., Bellouin, N., Decharme, B., Bopp, L., Brasika, I. B. M., Cadule, P., Chamberlain, M. A., Chandra, N., Chau, T. T. T., Chevallier, F., Chini, L. P., Cronin, M., Dou, X., Enyo, K., Evans, W., Falk, S., Feely, R. A., Feng, L., Ford, D. J., Gasser, T., Ghattas, J., Gkritzalis, T., Grassi, G., Gregor, L., Gruber, N., Gürses, Ö., Harris, I., Hefner, M., Heinke, J., Houghton, R. A., Hurtt, G. C., Iida, Y., Ilyina, T., Jacobson, A. R., Jain, A., Jarníková, T., Jersild, A., Jiang, F., Jin, Z., Joos, F., Kato, E., Keeling, R. F., Kennedy, D., Goldewijk, K. K., Knauer, J., Korsbakken, J. I., Körtzinger, A., Lan, X., Lefèvre, N., Li, H., Liu, J., Liu, Z., Ma, L., Marland, G., Mayot, N., McGuire, P. C., McKinley, G. A., Meyer, G., Morgan, E. J., Munro, D. R., Nakaoka, S. I., Niwa, Y., O'Brien, K. M., Olsen, A., Omar, A. M., Ono, T., Paulsen, M., Pierrot, D., Pocock, K., Poulter, B., Powis, C. M., Rehder, G., Resplandy, L., Robertson, E., Rödenbeck, C.,

Rosan, T. M., Schwinger, J., Séférian, R., et al.: Global Carbon Budget 2023, Earth Syst. Sci. Data, 15, 5301–5369, https://doi.org/10.5194/essd-15-5301-2023, 2023.

Gelaro, R.: The modern-era retrospective analysis for research and applications, Version 2 (MERRA-2), J Climate, 30, https://doi.org/10.1175/JCLI-D-16-0758.1, 2017.

Gerbig, C., Lin, J. C., Wofsy, S. C., Daube, B. C., Andrews, A. E., Stephens, B. B., Bakwin, P. S., and Grainger, C. A.: Toward constraining regional-scale fluxes of CO2 with atmospheric observations over a continent: 2. Analysis of COBRA data using a receptor-oriented framework, Journal of Geophysical Research: Atmospheres, 108, https://doi.org/10.1029/2003jd003770, 2003.

Gilfillan, D. and Marland, G.: CDIAC-FF: Global and national CO2 emissions from fossil fuel combustion and cement manufacture: 1751-2017, Earth Syst. Sci. Data, 13, 1667–1680, https://doi.org/10.5194/essd-13-1667-2021, 2021.

Gurney, K. R., Law, R. M., Denning, A. S., Rayner, P. J., Baker, D., Bousquet, P., Bruhwiler, L., Chen, Y.-H., Ciais, P., Fan, S., Fung, I. Y., Gloor, M., Heimann, M., Higuchi, K., John, J., Maki, T., Maksyutov, S., Masarie, K., Peylin, P., Prather, M., Pak, B. C., Randerson, J., Sarmiento, J., Taguchi, S., Takahashi, T., and Yuen, C.-W.: Towards robust regional estimates of CO2 sources and sinks using atmospheric transport models, Nature, 415, 626–630, https://doi.org/10.1038/415626a, 2002.

Gurney, K. R., Law, R. M., Denning, A. S., Rayner, P. J., Baker, D., Bousquet, P., Bruhwiler, L., Chen, Y.-H., Ciais, P., Fan, S., Fung, I. Y., Gloor, M., Heimann, M., Higuchi, K., John, J., Kowalczyk, E., Maki, T., Maksyutov, S., Peylin, P., Prather, M., Pak, B. C., Sarmiento, J., Taguchi, S., Takahashi, T., and Yuen, C.-W.: TransCom 3 CO 2 inversion intercomparison: 1. Annual mean control results and sensitivity to transport and prior flux information, 55, 555–579, 2003.

Hersbach, H., Bell, B., Berrisford, P., Hirahara, S., Horányi, A., Muñoz-Sabater, J., Nicolas, J., Peubey, C., Radu, R., Schepers, D., Simmons, A., Soci, C., Abdalla, S., Abellan, X., Balsamo, G., Bechtold, P., Biavati, G., Bidlot, J., Bonavita, M., De Chiara, G., Dahlgren, P., Dee, D., Diamantakis, M., Dragani, R., Flemming, J., Forbes, R., Fuentes, M., Geer, A., Haimberger, L., Healy, S., Hogan, R. J., Hólm, E., Janisková, M., Keeley, S., Laloyaux, P., Lopez, P., Lupu, C., Radnoti, G., de Rosnay, P., Rozum, I., Vamborg, F., Villaume, S., and Thépaut, J. N.: The ERA5 global reanalysis, Quarterly Journal of the Royal Meteorological Society, 146, 1999–2049, https://doi.org/10.1002/qj.3803, 2020.

Houweling, S., Baker, D., Basu, S., Boesch, H., Butz, A., Chevallier, F., Deng, F., Dlugokencky, E. J., Feng, L., Ganshin, A., Hasekamp, O., Jones, D., Maksyutov, S., Marshall, J., Oda, T., O'Dell, C. W., Oshchepkov, S., Palmer, P. I., Peylin, P., Poussi, Z., Reum, F., Takagi, H., Yoshida, Y., and Zhuravlev, R.: An intercomparison of inversemodels for estimating sources and sinks of CO2 using GOSAT measurements, J. Geophys. Res., 120, 5253–5266, https://doi.org/10.1002/2014JD022962, 2015.

Huete, A., Didan, K., Miura, T., Rodriguez, E. P., Gao, X., and Ferreira, L. G.: Overview of the radiometric and biophysical performance of the MODIS vegetation indices, https://doi.org/https://doi.org/10.1016/S0034-4257(02)00096-2, 2002.

Intergovernmental Panel on Climate Change (IPCC): Global Carbon and Other Biogeochemical Cycles and Feedbacks, in: Climate Change 2021 – The Physical Science Basis, Cambridge University Press, 673–816, https://doi.org/10.1017/9781009157896.007, 2023.

Jiang, F., Wang, H. W., Chen, J. M., Zhou, L. X., Ju, W. M., Ding, A. J., Liu, L. X., and Peters, W.: Nested atmospheric inversion for the terrestrial carbon sources and sinks in China, Biogeosciences, 10, 5311–5324, https://doi.org/10.5194/bg-10-5311-2013, 2013.

Jiang, F., Wang, H., Chen, J. M., Ju, W., Tian, X., Feng, S., Li, G., Chen, Z., Zhang, S., Lu, X., Liu, J., Wang, H., Wang, J., He, W., and Wu, M.: Regional CO2 fluxes from 2010 to 2015 inferred from GOSAT XCO2 retrievals using a new version of the Global Carbon Assimilation System, Atmos. Chem. Phys., 21, 1963–1985, https://doi.org/10.5194/acp-21-1963-2021, 2021.

Jiang, F., Ju, W., He, W., Wu, M., Wang, H., Wang, J., Jia, M., Feng, S., Zhang, L., and Chen, J. M.: A 10-year global monthly averaged terrestrial net ecosystem exchange dataset inferred from the ACOS GOSAT v9 XCO2retrievals (GCAS2021), Earth Syst. Sci. Data, 14, 3013–3037, https://doi.org/10.5194/essd-14-3013-2022, 2022a.

Jiang, P., Ding, W., Yuan, Y., Ye, W., and Mu, Y.: Interannual variability of vegetation sensitivity to climate in China, J. Environ. Manage., 301, https://doi.org/10.1016/j.jenvman.2021.113768, 2022b.

Jin, J., Lin, H. X., Heemink, A., and Segers, A.: Spatially varying parameter estimation for dust emissions using reduced-tangent-linearization 4DVar, Atmos. Environ., 187, 358–373, https://doi.org/10.1016/j.atmosenv.2018.05.060, 2018.

Joos, F. and Spahni, R.: Rates of change in natural and anthropogenic radiative forcing over the past 20,000 years, 2008.

Jung, M., Schwalm, C., Migliavacca, M., Walther, S., Camps-Valls, G., Koirala, S., Anthoni, P., Besnard, S., Bodesheim, P., Carvalhais, N., Chevallier, F., Gans, F., S Goll, D., Haverd, V., Köhler, P., Ichii, K., K Jain, A., Liu, J., Lombardozzi, D., E M S Nabel, J., A Nelson, J., O'Sullivan, M., Pallandt, M., Papale, D., Peters, W., Pongratz, J., Rödenbeck, C., Sitch, S., Tramontana, G., Walker, A., Weber, U., and Reichstein, M.: Scaling carbon fluxes from eddy covariance sites to globe: Synthesis and evaluation of the FLUXCOM approach, Biogeosciences, 17, 1343–1365, https://doi.org/10.5194/bg-17-1343-2020, 2020.

Kaminski, T., Scholze, M., and Houweling, S.: Quantifying the benefit of A-SCOPE data for reducing uncertainties in terrestrial carbon fluxes in CCDAS, Tellus B Chem. Phys. Meteorol., 62, 784–796, https://doi.org/10.1111/j.1600-0889.2010.00483.x, 2010.

Kondo, M., Patra, P. K., Sitch, S., Friedlingstein, P., Poulter, B., Chevallier, F., Ciais, P., Canadell, J. G., Bastos, A., Lauerwald, R., Calle, L., Ichii, K., Anthoni, P., Arneth, A., Haverd, V., Jain, A. K., Kato, E., Kautz, M., Law, R. M., Lienert, S., Lombardozzi, D., Maki, T., Nakamura, T., Peylin, P., Rödenbeck, C., Zhuravlev, R., Saeki, T., Tian, H., Zhu, D., and Ziehn, T.: State of the science in reconciling top-down and bottom-up approaches for terrestrial CO2 budget, Glob. Chang. Biol., 26, 1068–1084, https://doi.org/10.1111/gcb.14917, 2020.

Kou, X., Peng, Z., Zhang, M., Hu, F., Han, X., Li, Z., and Lei, L.: The carbon sink in China as seen from GOSAT with a regional inversion system based on the Community Multi-scale Air Quality (CMAQ) and ensemble Kalman smoother (EnKS), Atmos. Chem. Phys., 23, 6719–6741, https://doi.org/10.5194/acp-23-6719-2023, 2023.

Kulawik, S. S., Crowell, S., Baker, D., Liu, J., McKain, K., Sweeney, C., Biraud, S. C., Wofsy, S., O'Dell, C. W., Wennberg, P. O., Wunch, D., Roehl, C. M., Deutscher, N. M., Kiel, M., Griffith, D. W. T., Velazco, V. A., Notholt, J., Warneke, T., Petri,

C., De Mazière, M., Sha, M. K., Sussmann, R., Rettinger, M., Pollard, D. F., Morino, I., Uchino, O., Hase, F., Feist, D. G., Roche, S., Strong, K., Kivi, R., Iraci, L., Shiomi, K., Dubey, M. K., Sepulveda, E., Rodriguez, O. E. G., Té, Y., Jeseck, P., Heikkinen, P., Dlugokencky, E. J., Gunson, M. R., Eldering, A., Crisp, D., Fisher, B., and Osterman, G. B.: Characterization of OCO-2 and ACOS-GOSAT biases and errors for CO₂ flux estimates, https://doi.org/10.5194/amt-2019-257, 28 October 2019.

Lan, X., Tans, P., and K.W. Thoning: Trends in globally-averaged CO2 determined from NOAA Global Monitoring Laboratory measurements. Version Thursday, 05-Jun-2025 08:00:43 MDT, 2025.

Lian, Y., Li, H., Renyang, Q., Liu, L., Dong, J., Liu, X., Qu, Z., Lee, L. C., Chen, L., Wang, D., and Zhang, H.: Mapping the net ecosystem exchange of CO2 of global terrestrial systems, https://doi.org/10.1016/j.jag.2022.103176, 1 February 2023.

Liu, J., Baskaran, L., Bowman, K., Schimel, D., Anthony Bloom, A., Parazoo, C. N., Oda, T., Carroll, D., Menemenlis, D., Joiner, J., Commane, R., Daube, B., Gatti, V. L., McKain, K., Miller, J., Stephens, B. B., Sweeney, C., and Wofsy, S.: Carbon Monitoring System Flux Net Biosphere Exchange 2020 (CMS-Flux NBE 2020), Earth Syst. Sci. Data, 13, 299–330, https://doi.org/10.5194/essd-13-299-2021, 2021.

Liu, Y., Zhao, Y., Wu, W., Ao, X., and Chen, R.: The Response of Vegetation Dynamics to Climate in Xinjiang from 1991 to 2018, Forests, 15, https://doi.org/10.3390/f15122065, 2024.

Lu, B., Li, H., Wu, J., Zhang, T., Liu, J., Liu, B., Chen, Y., and Baishan, J.: Impact of El Niño and Southern Oscillation on the summer precipitation over Northwest China, Atmospheric Science Letters, 20, https://doi.org/10.1002/asl.928, 2019.

Ma, F., Ye, A., You, J., and Duan, Q.: 2015–16 floods and droughts in China, and its response to the strong El Niño, Science of the Total Environment, 627, 1473–1484, https://doi.org/10.1016/j.scitotenv.2018.01.280, 2018.

Monteil, G., Broquet, G., Scholze, M., Lang, M., Karstens, U., Gerbig, C., Koch, F. T., Smith, N. E., Thompson, R. L., Luijkx, I. T., White, E., Meesters, A., Ciais, P., Ganesan, A. L., Manning, A., Mischurow, M., Peters, W., Peylin, P., Tarniewicz, J., Rigby, M., Rödenbeck, C., Vermeulen, A., and Walton, E. M.: The regional European atmospheric transport inversion comparison, EUROCOM: First results on European-wide terrestrial carbon fluxes for the period 2006-2015, Atmos. Chem. Phys., 20, 12063–12091, https://doi.org/10.5194/acp-20-12063-2020, 2020.

Munassar, S., Rödenbeck, C., Koch, F. T., Totsche, K. U., Gałkowski, M., Walther, S., and Gerbig, C.: Net ecosystem exchange (NEE) estimates 2006-2019 over Europe from a pre-operational ensemble-inversion system, Atmos. Chem. Phys., 22, 7875–7892, https://doi.org/10.5194/acp-22-7875-2022, 2022.

Nassar, R., Jones, D. B. A., Suntharalingam, P., Chen, J. M., Andres, R. J., Wecht, K. J., Yantosca, R. M., Kulawik, S. S., Bowman, K. W., Worden, J. R., MacHida, T., and Matsueda, H.: Modeling global atmospheric CO2 with improved emission inventories and CO2 production from the oxidation of other carbon species, Geosci. Model Dev., 3, 689–716, https://doi.org/10.5194/gmd-3-689-2010, 2010.

Nassar, R., Jones, D. B. A., Kulawik, S. S., Worden, J. R., Bowman, K. W., Andres, R. J., Suntharalingam, P., Chen, J. M., Brenninkmeijer, C. A. M., Schuck, T. J., Conway, T. J., and Worthy, D. E.: Inverse modeling of CO2 sources and sinks using

satellite observations of CO2 from TES and surface flask measurements, Atmos. Chem. Phys., 11, 6029–6047, https://doi.org/10.5194/acp-11-6029-2011, 2011.

Nassar, R., Napier-Linton, L., Gurney, K. R., Andres, R. J., Oda, T., Vogel, F. R., and Deng, F.: Improving the temporal and spatial distribution of co2 emissions from global fossil fuel emission data sets, Journal of Geophysical Research Atmospheres, 118, 917–933, https://doi.org/10.1029/2012JD018196, 2013.

Noumonvi, K. D. and Ferlan, M.: Empirical vs. light-use efficiency modelling for estimating carbon fluxes in a mid-succession ecosystem developed on abandoned karst grassland, PLoS One, 15, https://doi.org/10.1371/journal.pone.0237351, 2020.

Oda, T. and Maksyutov, S.: A very high-resolution (1km×1 km) global fossil fuel CO2 emission inventory derived using a point source database and satellite observations of nighttime lights, Atmos. Chem. Phys., 11, 543–556, https://doi.org/10.5194/acp-11-543-2011, 2011.

Oda, T., Maksyutov, S., and Andres, R. J.: The Open-source Data Inventory for Anthropogenic CO2, version 2016 (ODIAC2016): A global monthly fossil fuel CO2 gridded emissions data product for tracer transport simulations and surface flux inversions, Earth Syst. Sci. Data, 10, 87–107, https://doi.org/10.5194/essd-10-87-2018, 2018.

O'Dell, C. W., Connor, B., Bösch, H., O'Brien, D., Frankenberg, C., Castano, R., Christi, M., Eldering, D., Fisher, B., Gunson, M., McDuffie, J., Miller, C. E., Natraj, V., Oyafuso, F., Polonsky, I., Smyth, M., Taylor, T., Toon, G. C., Wennberg, P. O., and Wunch, D.: The ACOS CO2 retrieval algorithm-Part 1: Description and validation against synthetic observations, Atmos. Meas. Tech., 5, 99–121, https://doi.org/10.5194/amt-5-99-2012, 2012.

Palmer, P. I., Jacob, D. J., Jones, D. B. A., Heald, C. L., Yantosca, R. M., Logan, J. A., Sachse, G. W., and Streets, D. G.: Inverting for emissions of carbon monoxide from Asia using aircraft observations over the western Pacific, Journal of Geophysical Research: Atmospheres, 108, https://doi.org/10.1029/2003jd003397, 2003.

Park, J. and Kim, H. M.: Design and evaluation of CO2 observation network to optimize surface CO2 fluxes in Asia using observation system simulation experiments, Atmos. Chem. Phys., 20, 5175–5195, https://doi.org/10.5194/acp-20-5175-2020, 2020.

Patra, P. K., Hajima, T., Saito, R., Chandra, N., Yoshida, Y., Ichii, K., Kawamiya, M., Kondo, M., Ito, A., and Crisp, D.: Evaluation of earth system model and atmospheric inversion using total column CO2 observations from GOSAT and OCO-2, Prog. Earth Planet. Sci., 8, https://doi.org/10.1186/s40645-021-00420-z, 2021.

Peters, W., Jacobson, A. R., Sweeney, C., Andrews, A. E., Conway, T. J., Masarie, K., Miller, J. B., P Bruhwiler, L. M., Pé tron, G., Hirsch, A. I., J Worthy, D. E., van der Werf, G. R., Randerson, J. T., Wennberg, P. O., Krol, M. C., and Tans, P. P.: An atmospheric perspective on North American carbon dioxide exchange: CarbonTracker, 2007.

Peylin, P., Law, R. M., Gurney, K. R., Chevallier, F., Jacobson, A. R., Maki, T., Niwa, Y., Patra, P. K., Peters, W., Rayner, P. J., Rödenbeck, C., Van Der Laan-Luijkx, I. T., and Zhang, X.: Global atmospheric carbon budget: Results from an ensemble of atmospheric CO2 inversions, Biogeosciences, 10, 6699–6720, https://doi.org/10.5194/bg-10-6699-2013, 2013.

Potithep, S., Nagai, S., Nasahara, K. N., Muraoka, H., and Suzuki, R.: Two separate periods of the LAI-VIs relationships using in situ measurements in a deciduous broadleaf forest, Agric. For. Meteorol., 169, 148–155, https://doi.org/10.1016/j.agrformet.2012.09.003, 2013.

Randerson, J. T., van der Werf, G. R., Giglio, L., Collatz, G. J., and Kasibhatla, P. S.: Global Fire Emissions Database, Version 4.1 (GFEDv4), 2018.

Reichstein, M., Falge, E., Baldocchi, D., Papale, D., Aubinet, M., Berbigier, P., Bernhofer, C., Buchmann, N., Gilmanov, T., Granier, A., Grünwald, T., Havránková, K., Ilvesniemi, H., Janous, D., Knohl, A., Laurila, T., Lohila, A., Loustau, D., Matteucci, G., Meyers, T., Miglietta, F., Ourcival, J. M., Pumpanen, J., Rambal, S., Rotenberg, E., Sanz, M., Tenhunen, J., Seufert, G., Vaccari, F., Vesala, T., Yakir, D., and Valentini, R.: On the separation of net ecosystem exchange into assimilation and ecosystem respiration: Review and improved algorithm, https://doi.org/10.1111/j.1365-2486.2005.001002.x, September 2005.

Ren, H. L., Wang, R., Zhai, P., Ding, Y., and Lu, B.: Upper-ocean dynamical features and prediction of the super El Niño in 2015/16: A comparison with the cases in 1982/83 and 1997/98, Journal of Meteorological Research, 31, 278–294, https://doi.org/10.1007/s13351-017-6194-3, 2017.

Rodgers, C. D.: Inverse methods for atmospheric sounding: theory and practice, World scientific, 2000.

Schourup-Kristensen, V., Wekerle, C., Wolf-Gladrow, D. A., and Völker, C.: Arctic Ocean biogeochemistry in the high resolution FESOM 1.4-REcoM2 model, Prog. Oceanogr., 168, 65–81, https://doi.org/10.1016/j.pocean.2018.09.006, 2018.

Sitch, S., Huntingford, C., Gedney, N., Levy, P. E., Lomas, M., Piao, S. L., Betts, R., Ciais, P., Cox, P., Friedlingstein, P., Jones, C. D., Prentice, I. C., and Woodward, F. I.: Evaluation of the terrestrial carbon cycle, future plant geography and climate-carbon cycle feedbacks using five Dynamic Global Vegetation Models (DGVMs), Glob. Chang. Biol., 14, 2015–2039, https://doi.org/10.1111/j.1365-2486.2008.01626.x, 2008.

Sitch, S., Friedlingstein, P., Gruber, N., Jones, S. D., Murray-Tortarolo, G., Ahlström, A., Doney, S. C., Graven, H., Heinze, C., Huntingford, C., Levis, S., Levy, P. E., Lomas, M., Poulter, B., Viovy, N., Zaehle, S., Zeng, N., Arneth, A., Bonan, G., Bopp, L., Canadell, J. G., Chevallier, F., Ciais, P., Ellis, R., Gloor, M., Peylin, P., Piao, S. L., Le Quéré, C., Smith, B., Zhu, Z., and Myneni, R.: Recent trends and drivers of regional sources and sinks of carbon dioxide, Biogeosciences, 12, 653–679, https://doi.org/10.5194/bg-12-653-2015, 2015.

Suntharalingam, P., Jacob, D. D., Palmer, P. I., Logan, J. A., Yantosca, R. M., Xiao, Y., Evans, M. J., Streets, D. G., Vay, S. L., and Sachse, G. W.: Improved quantificaion of Chinese carbon fluxes using CO2/CO correlations in Asian outflow, Journal of Geophysical Research Atmospheres, 109, https://doi.org/10.1029/2003JD004362, 2004.

Takagi, H., Saeki, T., Oda, T., Saito, M., Valsala, V., Belikov, D., Saito, R., Yoshida, Y., Morino, I., Uchino, O., Andres, R. J., Yokota, T., and Maksyutov, S.: On the benefit of GOSAT observations to the estimation of regional CO2 fluxes, Scientific Online Letters on the Atmosphere, 7, 161–164, https://doi.org/10.2151/sola.2011-041, 2011.

Taylor, T. E., O'Dell, C. W., Crisp, D., Kuze, A., Lindqvist, H., Wennberg, P. O., Chatterjee, A., Gunson, M., Eldering, A., Fisher, B., Kiel, M., Nelson, R. R., Merrelli, A., Osterman, G., Chevallier, F., Palmer, P. I., Feng, L., Deutscher, N. M., Dubey,

M. K., Feist, D. G., García, O. E., Griffith, D. W. T., Hase, F., Iraci, L. T., Kivi, R., Liu, C., De Mazière, M., Morino, I., Notholt, J., Oh, Y. S., Ohyama, H., Pollard, D. F., Rettinger, M., Schneider, M., Roehl, C. M., Sha, M. K., Shiomi, K., Strong, K., Sussmann, R., Té, Y., Velazco, V. A., Vrekoussis, M., Warneke, T., and Wunch, D.: An 11-year record of XCO2 estimates derived from GOSAT measurements using the NASA ACOS version 9 retrieval algorithm, Earth Syst. Sci. Data, 14, 325–360, https://doi.org/10.5194/essd-14-325-2022, 2022.

Thompson, R. L., Patra, P. K., Chevallier, F., Maksyutov, S., Law, R. M., Ziehn, T., Van Der Laan-Luijkx, I. T., Peters, W., Ganshin, A., Zhuravlev, R., Maki, T., Nakamura, T., Shirai, T., Ishizawa, M., Saeki, T., Machida, T., Poulter, B., Canadell, J. G., and Ciais, P.: Top-down assessment of the Asian carbon budget since the mid 1990s, Nat. Commun., 7, https://doi.org/10.1038/ncomms10724, 2016.

Tian, H., Chen, G., Liu, M., Zhang, C., Sun, G., Lu, C., Xu, X., Ren, W., Pan, S., and Chappelka, A.: Model estimates of net primary productivity, evapotranspiration, and water use efficiency in the terrestrial ecosystems of the southern United States during 1895-2007, For. Ecol. Manage., 259, 1311–1327, https://doi.org/10.1016/j.foreco.2009.10.009, 2010.

Tolk, L. F., Meesters, A. G. C. A., Dolman, A. J., and Peters, W.: Modelling representation errors of atmospheric CO 2 mixing ratios at a regional scale, Atmos. Chem. Phys, 6587–6596 pp., 2008.

UNFCCC: Paris Agreement, 2015.

Wang, H., Jiang, F., Wang, J., Ju, W., and Chen, J. M.: Terrestrial ecosystem carbon flux estimated using GOSAT and OCO-2 XCO2 retrievals, Atmos. Chem. Phys., 19, 12067–12082, https://doi.org/10.5194/acp-19-12067-2019, 2019.

Wang, J., Feng, L., Palmer, P. I., Liu, Y., Fang, S., Bösch, H., O'Dell, C. W., Tang, X., Yang, D., Liu, L., and Xia, C. Z.: Large Chinese land carbon sink estimated from atmospheric carbon dioxide data, Nature, 586, 720–723, https://doi.org/10.1038/s41586-020-2849-9, 2020.

Wang, W., Ciais, P., Nemani, R. R., Canadell, J. G., Piao, S., Sitch, S., White, M. A., Hashimoto, H., Milesi, C., and Myneni, R. B.: Variations in atmospheric CO2 growth rates coupled with tropical temperature, Proc. Natl. Acad. Sci. U. S. A., 110, 13061–13066, https://doi.org/10.1073/pnas.1219683110, 2013.

Wang, X., Piao, S., Ciais, P., Friedlingstein, P., Myneni, R. B., Cox, P., Heimann, M., Miller, J., Peng, S., Wang, T., Yang, H., and Chen, A.: A two-fold increase of carbon cycle sensitivity to tropical temperature variations, Nature, 506, 212–215, https://doi.org/10.1038/nature12915, 2014.

Wang, X., Gao, Y., Jeong, S., Ito, A., Bastos, A., Poulter, B., Wang, Y., Ciais, P., Tian, H., Yuan, W., Chandra, N., Chevallier, F., Fan, L., Hong, S., Lauerwald, R., Li, W., Lin, Z., Pan, N., Patra, P. K., Peng, S., Ran, L., Sang, Y., Sitch, S., Takashi, M., Thompson, R. L., Wang, C., Wang, K., Wang, T., Xi, Y., Xu, L., Yan, Y., Yun, J., Zhang, Y., Zhang, Y., Zhang, Z., Zheng, B., Zhou, F., Tao, S., Canadell, J. G., and Piao, S.: The Greenhouse Gas Budget of Terrestrial Ecosystems in East Asia Since 2000, Global Biogeochem. Cycles, 38, https://doi.org/10.1029/2023GB007865, 2024.

WMO: Wmo statement on the state of the global climate in 2016, WORLD METEOROLOGICAL ORG, Geneva, 2017.

Worden, R. J., Doran, G., Kulawik, S., Eldering, A., Crisp, D., Frankenberg, C., O'Dell, C., and Bowman, K.: Evaluation and attribution of OCO-2 XCO2 uncertainties, Atmos. Meas. Tech., 10, 2759–2771, https://doi.org/10.5194/amt-10-2759-2017, 2017.

Wu, Z., Lu, W., Roobaert, A., Song, L., Yan, X.-H., and Cai, W.-J.: A machine-learning reconstruction of sea surface pCO_2 in the North American Atlantic Coastal Ocean Margin from 1993 to 2021, Earth Syst. Sci. Data, 17, 43–63, https://doi.org/10.5194/essd-17-43-2025, 2025.

Wunch, D., Toon, G. C., Blavier, J.-F. L., Washenfelder, R. A., Notholt, J., Connor, B. J., Griffith, D. W. T., Sherlock, V., and Wennberg, P. O.: The Total Carbon Column Observing Network, Philosophical Transactions of the Royal Society A: Mathematical, Physical and Engineering Sciences, 369, 2087–2112, https://doi.org/10.1098/rsta.2010.0240, 2011.

Yeh, S. W., Shin, M. S., Ma, S. J., Kug, J. S., and Moon, B. K.: Understanding elevated CO2 concentrations in East Asia relative to the global mean during boreal spring on the slow and interannual timescales, Science of the Total Environment, 901, https://doi.org/10.1016/j.scitotenv.2023.166098, 2023.

You, Y., Tian, H., Pan, S., Shi, H., Bian, Z., Gurgel, A., Huang, Y., Kicklighter, D., Liang, X. Z., Lu, C., Melillo, J., Miao, R., Pan, N., Reilly, J., Ren, W., Xu, R., Yang, J., Yu, Q., and Zhang, J.: Incorporating dynamic crop growth processes and management practices into a terrestrial biosphere model for simulating crop production in the United States: Toward a unified modeling framework, Agric. For. Meteorol., 325, https://doi.org/10.1016/j.agrformet.2022.109144, 2022.

Yue, C., Ciais, P., Bastos, A., Chevallier, F., Yin, Y., Rödenbeck, C., and Park, T.: Vegetation greenness and land carbon-flux anomalies associated with climate variations: A focus on the year 2015, Atmos. Chem. Phys., 17, 13903–13919, https://doi.org/10.5194/acp-17-13903-2017, 2017.

Zhai, P., Yu, R., Guo, Y., Li, Q., Xuejuan, R., Wang, Y., Liu, Y., and Yihui, D.: The Strong El Niño of 2015/16 and Its Dominant Impacts on Global and China's Climate, J. Meteor. Res, 30, 283–297, https://doi.org/10.1007/s13, 2016.

Zhu, H. and Tan, Y.: The Origin of Evergreen Broad-Leaved Forests in East Asia from the Evidence of Floristic Elements, https://doi.org/10.3390/plants13081106, 1 April 2024.